A Unified Theory for Porous Capacitive Pressure Sensors

Zhengjie Li, Zheliang Wang, Peiran Wei, Nanshu Lu

PII: S0022-5096(26)00192-4
DOI: https://doi.org/10.1016/j.jmps.2026.106691
Reference: MPS 106691

To appear in: *Journal of the Mechanics and Physics of Solids*

Received date: 7 March 2026
Revised date: 12 May 2026
Accepted date: 19 May 2026

Please cite this article as: Zhengjie Li, Zheliang Wang, Peiran Wei, Nanshu Lu, A Unified Theory for Porous Capacitive Pressure Sensors, *Journal of the Mechanics and Physics of Solids* (2025), doi: https://doi.org/10.1016/j.jmps.2026.106691

A Unified Theory for Porous Capacitive Pressure Sensors

Zhengjie Li[a,1], Zheliang Wang[a,1], Peiran Wei[b], Nanshu Lu[a,c,d,e,f,*]

[a] *Department of Aerospace Engineering and Engineering Mechanics, the University of Texas at Austin, TX 78712,USA.*
[b] *Soft Matter Facility, Texas A&M University, College Station, Texas, USA, College Station, TX 77840*
[c] *Department of Biomedical Engineering, the University of Texas at Austin, TX 78712,USA.*
[d] *The Chandra Family Department of Electrical and Computer Engineering, the University of Texas at Austin, TX 78712,USA.*
[e] *Walker Department of Mechanical Engineering, the University of Texas at Austin, TX 78712,USA.*
[f] *Texas Materials Institute, the University of Texas at Austin, TX 78712,USA.*

Abstract

Capacitive pressure sensors (CPS) are widely used in robotics, prosthetics, biomimetics, and biosensing. Existing CPS—including those with engineered dielectrics, engineered electrodes, and hybrid capacitive–resistive responses—are modeled separately and therefore lack generalizable design rules. In this work, we develop a unified analytical model that captures concurrent capacitive and resistive transduction in CPS with porous sensing layers, whose dielectric loss can span the full possible range. The model yields a closed-form solution for CPS sensitivity in terms of five material and structural parameters. Experimental validation is performed using a porous nanocomposite (PNC) with varying conductive filler doping ratios and dielectric layer thicknesses. The analysis reveals that (i) the dielectric loss of the PNC is a dominant yet previously understudied performance descriptor; (ii) CPS sensitivity is also controlled by the thickness ratio between the porous sensing layer and the dielectric layer; and (iii) with everything else fixed, there is an optimal filler concentration for maximal CPS sensitivity. This framework unifies disparate dielectric losses of the porous media, unveils the fundamental connection and difference of various types of CPS, and ultimately provides simple guidance for the material–structural optimization of CPS.

Keywords: Flexible electronics, pressure sensors, e-skin, dielectric loss, piezoresistivity, capacitive

---

1. Introduction

Electronic skins (e-skins) are artificial devices designed to replicate the mechanical properties and sensory functions of human skin (Chortos et al., 2016). E-skins have drawn significant attention in recent years due to their increasing importance in various growing technologies, such as humanoids, soft robotics, prosthetics, and biomedical sensors (Yao and Zhu, 2014; Dahiya et al., 2013; Chortos et al., 2016; Lee et al., 2019; Wang et al., 2021b; Pyo et al., 2021a). Pressure sensors, the central component of e-skin, have been extensively studied, leading to the development of multiple sensing mechanisms, including resistive (Lee et al., 2016; Liu

---

[*] Corresponding author
Email address: `nanshulu@utexas.edu` (Nanshu Lu)
[1] Co-first authors

et al., 2017; Lee et al., 2018; Zhao et al., 2019; He et al., 2020), capacitive (Mannsfeld et al., 2010; Viry et al., 2014; Park et al., 2014; Ha et al., 2021, 2024), iontronic (Li et al., 2017; Bai et al., 2020, 2022; Xiong et al., 2022), piezoelectric (Chorsi et al., 2019; Chun et al., 2014; Choi et al., 2014), triboelectric (Garcia et al., 2018), optical (Ramuz et al., 2012; Yamada et al., 2005), and magnetoelastic (Man et al., 2022) sensing. Each mechanism offers unique advantages and drawbacks, as reviewed in Pyo et al. (2021b); Meng et al. (2022); Nie et al. (2024). In this work, we focus on capacitive pressure sensors (CPS), which have gained popularity due to their high sensitivity, ease of fabrication and signal readout, long-term mechanical and electrical stability, and low power consumption (Chen and Yan, 2020; Li et al., 2020a; Qin et al., 2021; Yuan et al., 2021; Yang et al., 2020; Duan et al., 2022; Yang et al., 2017).

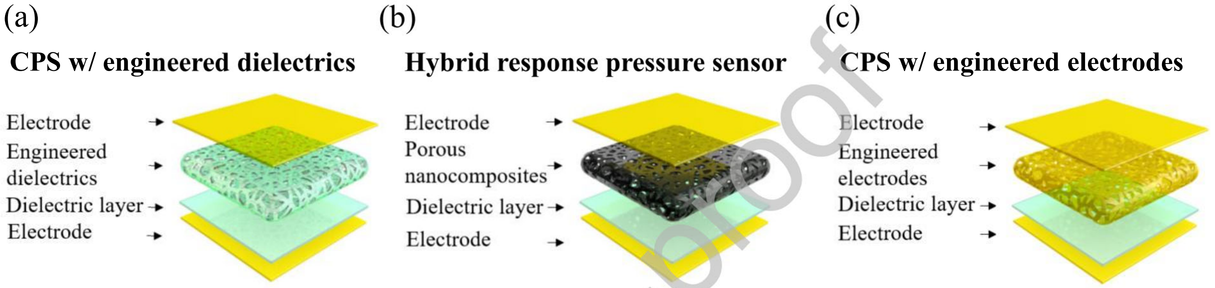

Figure 1: Schematics of three representative types of capacitive pressure sensors (CPS): (a) CPS with engineered dielectrics; (b) Hybrid response pressure sensor (HRPS); (c) CPS with engineered electrodes.

Various structural engineering strategies have been proposed to enhance the performance of CPS (Ha et al., 2022; Mishra et al., 2021b; Meng et al., 2022). In addition to varying mechanical properties, electrical properties such as dielectric loss can be easily tuned. Dielectric loss represents the conversion of electrical energy into heat within an insulating material as its internal dipoles struggle to keep pace with a rapidly oscillating electric field. In an electrical circuit, dielectric loss is the dissipation of energy through a parallel resistive component (R) in an otherwise ideal capacitor (C). Depending on the dielectric loss of the sensing layer, CPS can be categorized into three types, as illustrated in Fig. 1: (i) CPS with engineered dielectrics, (ii) hybrid response pressure sensors (HRPS), and (iii) CPS with engineered electrodes. Qualitative electromechanical simulations shown in Fig. A.1 are included to help explain the three scenarios.

The most conventional CPS are those with engineered dielectrics. Examples include micro-pyramids (Mannsfeld et al., 2010), micro-domes (Zhang et al., 2017), and textile-inspired dielectric architectures (Liu et al., 2017). Most existing designs use only a single engineered dielectric layer without an additional dielectric layer (Ha et al., 2022), while some configurations place engineered dielectrics on a flat dielectric layer (Ruth et al., 2020). The two configurations exhibit similar capacitance responses when the flat dielectric layer is sufficiently thin and stiff relative to the engineered dielectric. In this work, we adopt the latter configuration (Fig. 1a) to ensure a consistent geometry for comparing the three types of CPS considered in this study.

Hybrid response pressure sensors (HRPS) (Fig. 1b) (Ha et al., 2021, 2024) are first constructed by laminating a barely conductive porous nanocomposite (PNC) and an ultrathin blanket dielectric layer between two parallel electrodes. The PNC is a highly porous open cell structure with tubular ligaments composed of carbon nanotube (CNT)-doped Ecoflex. When the CNT doping ratio approaches the percolation threshold, the PNC ligaments become somewhat conductive, and the air pores surrounded by such ligaments exhibit parasitic capacitance. As a result, the overall PNC is endowed with hybrid resistive and capacitive responses measured with alternating current (AC). The insertion of the ultrathin dielectric layer between the PNC and the bottom electrode prevents DC flow between the two electrodes and, therefore, stabilizes the measured capacitance signal of the whole device. Although initially demonstrated using PNC, HRPS (Ha et al., 2021, 2024) is a generic mechanism that has been successfully implemented in many different materials and structures, such as multi-walled carbon nanotube/polydimethylsiloxane (MWCNT/PDMS) composites (Feng et al., 2023) , fiber structures (Qu et al., 2023), and fabric structures (Xiao et al., 2026).

CPS with engineered electrodes (Fig. 1c) incorporates porous (Zhong et al., 2023) or microstructured (Zhang et al., 2019a) highly conductive materials placed on top of a flat dielectric layer supported by a bottom electrode. The flat electrode added atop the engineered electrode serves as a fully conductive current collector.

In this work, we limit our scope to pressure sensing layers with stochastic porous structures. However, the framework can potentially be extended to other types of structures, including microdomes, architected materials, and more. As illustrated in Fig. 1, once the structure is unified, the differences among the three types of CPS effectively reduce to differences in the dielectric loss of the porous materials. Doping, i.e., the introduction of conductive fillers into a pristine polymer matrix, is a common material-engineering strategy that can tune the dielectric loss of the PNC (Wang et al., 2021a). At zero or low doping ratios, the PNC behaves as a pure dielectric. Near the percolation threshold, it behaves like a leaky capacitor. At sufficiently high doping ratios, the PNC becomes highly conductive. This progression of the dielectric loss of the PNC offers a continuous material property tuning strategy that can be modeled by a unified theory (Fig. 1).

The overall impedance of all three types of CPS can be described by a complex parameter $\mathbf{Z} = |Z|e^{i\theta}$, where $|Z|$ is the magnitude of the impedance and θ is the phase angle. The impedance can be described equivalently as the parallel capacitance and resistance: $C_\mathrm{p} = \sin\theta/(\omega|Z|), R_\mathrm{p} = |Z|/\cos\theta$, where ω is the angular frequency of the applied AC excitation. While the phase angle reflects the relative contributions of capacitive and resistive responses, dielectric loss (via loss angle, δ, or loss tangent, $\tan\delta$) quantifies directly and conveniently how much energy is dissipated, making it the preferred description for material characterization and engineering design. δ can be related to θ through

$$\delta = 90^\circ + \theta. \tag{1}$$

An ideal capacitor corresponds to $\delta = 0^\circ$, while an ideal resistor corresponds to $\delta = 90^\circ$.

Figure 2 uses circuit models and impedance plots (red and blue for undeformed and compressed configurations, respectively) to illustrate the differences between the three types of CPS and the effects of the flat dielectric layer: Figs. 2(a-c) do not include it, while Figs. 2(d-f) do. Therefore, Figs. 2(a-c) are used for characterizing the electromechanical properties of the PNC, and Figs. 2(d-f) are the corresponding CPS.

As shown in Fig. 2a(i), engineered dielectrics can be modeled as a single capacitor C_p (Fig. 2a(ii)) (Pyo et al., 2021b; Li et al., 2020b; Qin et al., 2021; Mishra et al., 2021a; Ha et al., 2022). Under compression, the magnitude of the impedance decreases from $|Z|$ to $|Z'|$ with a constant phase angle $\theta \equiv -90°$ and loss angle $\delta \equiv 0°$ (Fig.2a(iii)). Moderately doped PNC in HRPS (Fig.2b(i)) (Ha et al., 2021, 2024; Wang et al., 2024) can be modeled as a parallel resistor-capacitor circuit (R_p and C_p) as shown in Fig.2b(ii). Upon compression, its phase angle and loss angle can change drastically, as shown in Fig.2b(iii), due to the order of magnitude change in the resistance of the PNC. Finally, CPS with engineered electrodes (Fig.2c(i)) incorporate a highly doped conductive sensing layer, with resistances typically ranging from a few ohms to several kilo-ohms (Zhong et al., 2023), which can be represented by a resistor R_p (Fig.2c(ii)), with a constant phase angle $\theta \equiv 0°$ (equivalently, a loss angle $\delta \equiv 90°$)(Fig.2c(iii)). PNCs show rich electromechanical properties, including strong frequency dependence and large piezoresistivity near the percolation threshold, which can be attributed to tunneling effects and Maxwell–Wagner–Sillars interfacial polarization (Xia et al., 2017; Lu et al., 2017). However, physics-based models typically involve many parameters that are difficult to obtain. In this work, we describe the electromechanical behavior using a phenomenological model.

When a blanket dielectric layer is added between the PNC and the bottom electrode (Fig. 2(d–f) (i)), the four-layer laminate forms a CPS. The thickness of the sensing layer is indicated by d_f, and that of the dielectric (or insulating) layer is indicated by d_i. The corresponding circuit models are shown in Figs. 2(d–f)(ii). For CPS with engineered dielectrics (Fig. 2d), the circuit model is a serial connection of the engineered dielectric capacitor C_p and the dielectric layer capacitor C_i. As a result, the electromechanical response of the sensor resembles that of the sensing material with minimal contribution from interfacial contacts, showing a decreasing magnitude of impedance and a constant phase angle.

HRPS (Fig. 2e) consists of two parallel branches: a resistive branch, in which the resistor R_p directly contacts a part of the dielectric layer, represented by the interfacial capacitance C_i1; and a capacitive branch, where the PNC capacitance C_p is coupled to the remaining capacitance of the dielectric layer C_i2. The sensor first exhibits a near pure capacitive response $\theta \approx -90°$ (loss angle $\delta \approx 0°$). Upon compression, due to the blanket dielectric layer, the sensor will remain capacitive, showing a decrease in impedance $|Z'|$ and an increase in phase angle θ' greater than 0° (loss angle δ' less than 90°). In contrast to CPS with an engineered dielectric, the capacitance response in HRPS comes from both the bulk deformation of the PNC and the change in interfacial contacts between the PNC and the flat dielectric layer (Fig. A.1a(ii)). More detailed discussions are offered in Appendix A.

For CPS with engineered electrodes (Fig. 2f), the equivalent circuit consists of a resistive element R_p in series with a portion of the dielectric capacitance, denoted as $C_\mathrm{i1} = \alpha C_\mathrm{i}$, which corresponds to the fraction of the actual solid–solid contact area (α) between the porous electrode and the dielectric layer. The resistive element R_p changes under compression, while the variation in the measured capacitance primarily arises from changes in the interfacial contact ratio α between the engineered electrode and the flat dielectric layer.(Figs. A.1a(iii) & A.1b). Under compression, α increases, causing the magnitude of the impedance to decrease, while the phase angle shifts from θ to θ' (or equivalently from δ to δ'), both away from 0° and 90°.

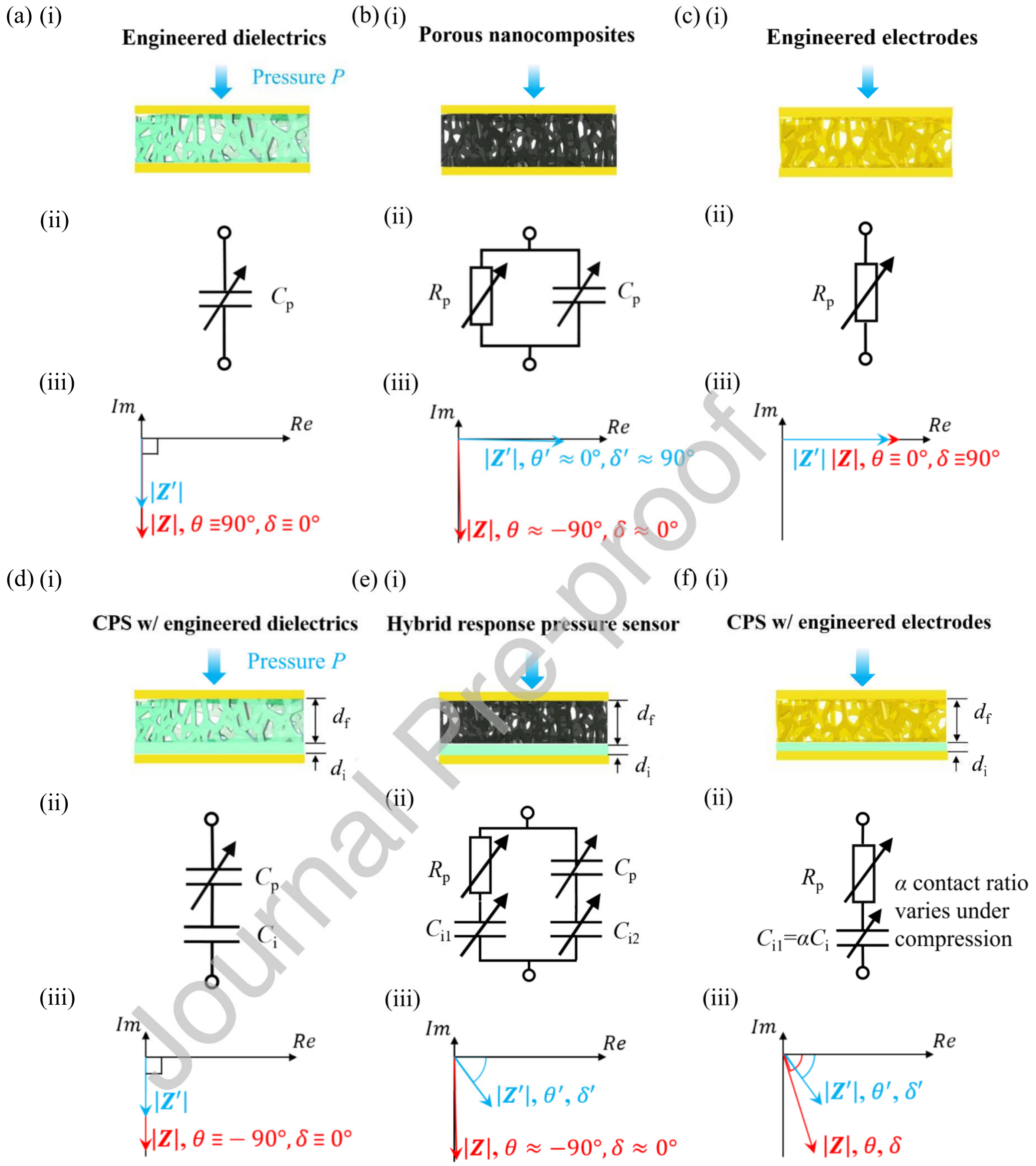

Figure 2: (a–c) Comparison of three representative sensing layers without a blanket dielectric layer. (a) Engineered dielectrics. (i) Schematics. (ii) The corresponding equivalent circuit consists of C_p. (iii) Under compression, the impedance decreases from $|Z|$ to $|Z'|$, while the phase angle (loss angle) remains the ideal capacitive limit of $-90°$ $(0°)$. (b) Porous nanocomposites. (i) Schematics. (ii) The equivalent circuit consists of a resistor R_p in parallel with a capacitor C_p. (iii) In the undeformed state, the phase angle (loss angle) is close to the ideal capacitive limit of $-90°$ $(0°)$. Under compression, the phase angle (loss angle) shifts toward the resistive limit of $0°$ $(90°)$, accompanied by a change in the magnitude of the impedance from $|Z|$ to $|Z'|$. (c) Engineered electrodes. (i) Schematics. (ii) The equivalent circuit is primarily resistive, governed by the resistance R_p. (iii) Under compression, the the magnitude of the impedance decreases from $|Z|$ to $|Z'|$, while the phase angle (loss angle) remains the ideal resistive limit of $0°$ $(90°)$.

Figure 2: (d–f) Comparison of three representative capacitive pressure sensors with a blanket dielectric layer. (d) CPS with engineered dielectrics. (i) Schematic illustration. (ii) The equivalent circuit consists of a parallel-plate capacitance formed between the top and bottom electrodes. (iii) Under compression, the magnitude of the impedance decreases from $|Z|$ to $|Z'|$, while the phase angle (loss angle) remains at the ideal capacitive limit of $-90°$ ($0°$). (e) Hybrid response pressure sensor (HRPS). (i) Schematic illustration (d_f and d_i represent the thickness of the foam and insulator, respectively). (ii) The equivalent circuit consists of two parallel branches, capturing the coexistence of piezoresistive branch (R_p and C_i1) and piezocapacitive branch (C_p and C_i2). (iii) As a result, the impedance evolve from $|Z|$ to $|Z'|$ and the phase angle (loss angle) shifting from near the ideal capacitive limit of $-90°$ ($0°$) toward an intermediate value between the capacitive and resistive limits. (f) CPS with engineered electrodes. (i) Schematic illustration. (ii) The equivalent circuit is governed by a resistive element R_p in series with an effective interfacial capacitance $C_\mathrm{i1} = \alpha C_\mathrm{i}$, where the contact ratio α increases under compression, as highlighted by the orange region. (iii) Compression leads to a decrease in magnitude of the impedance from $|Z|$ to $|Z'|$, accompanied by a phase-angle shift away from the ideal resistive limit.

Table 1 summarizes the three types of CPS illustrated in Fig. 2(d–f)(i) reported in the literature, comparing their constituent material properties, doping levels, structures (expressed through the thickness ratio $d_\mathrm{f}/d_\mathrm{i}$), and sensitivity. Despite the abundant literature, we notice that the definitions and differentiations of these CPS categories remain loosely established, resulting in inconsistent interpretations and even contradictions when comparing CPS of different categories. For example, CPS with engineered dielectrics with markedly different $d_\mathrm{f}/d_\mathrm{i}$ ratios (0.3175, 0.916, and 3.66) exhibit similar sensitivities of approximately 0.02 kPa^{-1} (Ruth et al., 2020). In contrast, CPS with engineered electrodes demonstrates improved sensitivity from 0.008 to 0.02 kPa^{-1} as the thickness ratio increases from 0.044 to 0.133 (Totaro et al., 2020). So far, there is no explanation for the different effects of $d_\mathrm{f}/d_\mathrm{i}$ in different types of CPS. In another example, the effects of the conductive filler doping ratio on sensitivity are non-monotonic: increasing the filler content initially enhances the sensitivity but eventually decreases it. Therefore, there is an optimal doping concentration at which the sensitivity is maximized (Ha et al., 2021, 2024; Zhong et al., 2023; He et al., 2023). Despite this well-known trend, doping ratios in most studies remain empirically chosen, with limited quantitative justification. As a result, CPS design continues to rely heavily on trial-and-error approaches, which are inherently time-consuming and wasteful of materials.

These gaps highlight the need for a unified theory that can provide fundamental understanding and quantitative prediction of the electromechanical behaviors of different types of CPS. Existing work includes empirical fitting expressions (Bilent et al., 2019), finite element simulations (Zhang et al., 2019b), and analytical models (Tee et al., 2014; Peng et al., 2018; Javidi et al., 2023). However, these models typically only work for one type of CPS and do not consider the effect of material engineering, such as the doping ratio. Previously, we developed a series of equivalent circuit models for HRPS ((Ha et al., 2021; Li et al., 2022; Wang et al., 2024)) that successfully captured the electromechanical behaviors of CPS with various doping ratios and measuring AC frequencies. However, these models are not generic enough to describe all three types of CPS and cannot offer an explicit expression for HRPS sensitivity as a function of material properties, such as doping ratios. To optimize the material composition for the highest sensitivity, we need

Reference	Type	Material	Doping ratio	Constituent material modulus	d_f / d_i (ratio)	Sensitivity [kPa^{-1}] (range [kPa])
Ruth et al., 2020a	CPS w/ engineered dielectric	PDMS	--	1.2 MPa	55 μm / 173 μm (0.3175)	0.022 (0-5)
					55 μm / 60 μm (0.916)	0.020 (0-5)
					55 μm / 15 μm (3.66)	0.021 (0-5)
Masihi et al., 2021	CPS w/ engineered dielectric	PDMS	--	1.2 MPa	--	~0.0107 (0-20) ~0.0084 (20-200) ~0.0032 (200-1000)
Ha et al., 2021	HRPS	CNT/Ecoflex	0%	70 kPa	650 μm / 500 nm (1300)	0.47* (0-1)
			0.25%			1.52* (0-1)
			0.5%			3.13 (0-1)
			0.75%			2.01* (0-1)
			1.0%			1.03* (0-1)
Ha et al., 2024	HRPS	CNT/Ecoflex	0%	70 kPa	900 μm / 2 μm (450)	0.41* (0-1)
			0.20%			0.85* (0-1)
			0.40%			2.13 (0-1)
			0.60%			1.32* (0-1)
			0.80%			1.03* (0-1)
Zhong et al., 2023	CPS w/ engineered electrodes	CNT/PDMS	10%	1.2 MPa	650 μm / 8 μm (81.25)	0.35* (0-1)
			12%			0.62* (0-1)
			15%			1.03 (0-1)
			17%			0.61* (0-1)
Totaro et al., 2020	CPS w/ engineered electrodes	PEDOT:PSS /PU	95% PEDOT:PSS 5% DMOSO	1 MPa	0.53 mm / 12 mm (0.044)	0.008 (0-3.5)
					0.53 mm / 8 mm (0.066)	0.01 (0-4)
					0.53 mm / 4 mm (0.133)	0.02 (0-2)

Table 1: Comparison of reported CPS with engineered dielectrics, HRPS, and CPS with engineered electrodes. d_f is the thickness of the porous sensing layer (f stands for foam), d_i is the thickness of the dielectric layer (i stands for insulator). Sensitivity values with * are calculated though the two point linear regression in normalized capacitance vs. pressure curve provided in the corresponding reference.

to establish a model that covers the full range of dielectric loss of the PNC sensing layer.

In this paper, we propose a generalized circuit model that is applicable to all three types of CPS with a PNC of a stochastic structure. Unlike most existing analytical models, which implicitly assume a zero loss angle, the framework first identifies the loss angle as a key indicator to accurately differentiate the three CPS types. CPS sensitivity is analytically expressed as a function of the PNC doping ratio and the thicknesses of the PNC and the dielectric layer. This result is experimentally validated. It can not only offer mechanistic explanations for experimental results reported in the literature but also predict the optimal sensor designs with minimal experimental effort.

The remainder of this paper is organized as follows. Section 2 presents the analytical model as well as the experimental fabrication and characterization protocols. Section 3 reports and discusses the results, focusing on the predictive capacity of the model with respect to the varying doping ratios, AC frequencies used for impedance measurement, and thicknesses of the layers. Section 4 concludes the work and outlines potential future directions.

2. Methods

2.1. Experimental methods

2.1.1. Sample preparation

We used a well-established fabrication method to prepare porous nanocomposites (PNC) (Ha et al., 2021, 2024). Carbon nanotubes with oxygen functionalized multiwall carbon nanotubes (MWCNTs, Carbon Nanotubes Plus) were dispersed in 240 mL of chloroform (Sigma-Aldrich) at varying masses—0, 60, 120, 180 and 240 mg— corresponding to doping ratios (by weight) of 0%, 0.2%, 0.4%, 0.6%, and 0.8%, respectively. The dispersion was ultrasonicated using a Q500 sonicator (QSonica) at 500 W for 10 minutes. Next, 30 g (weight ratio, A:B=1:1) of uncured Ecoflex (Ecoflex 00–30, Smooth-On) was added to the dispersion, followed by an additional 10-minute sonication. To evaporate chloroform, the mixture was heated and stirred at 100 °C and 400 rpm (Fisher Scientific magnetic stirrer) until the chloroform-to-Ecoflex weight ratio was reduced to 10:1. A 20 × 20 mm^2 nickel foam template was dip-coated in solution for 5 seconds, withdrawn, and placed on a hot plate of 150 °C for 10 minutes to evaporate chloroform. The dip-coating step was repeated once more, followed by curing in a 150 °C oven. After curing, the samples were etched in 1 M hydrochloric acid (HCl, Sigma-Aldrich) at 80 °C for 12 hours to dissolve the nickel foam, and then thoroughly rinsed with distilled water. The final samples were cut to 10 × 10 mm^2 for use in the characterization experiments.

2.1.2. Electrodes and dielectric layer fabrication

The copper electrodes were laser-cut into a 1 cm × 1 cm square shape with an attached 2 mm tail, according to a custom-designed CAD file. To systematically vary the thickness of the dielectric layer, we employ four fabrication methods to obtain dielectric layers with a thickness of 2 µm, 20 µm, 200 µm, 2000 µm. The dielectric layer with thickness of 2 µm was fabricated by mixing hexane and PDMS (monomer:crosslinker = 10:1) in a weight ratio of 4:1, followed by spin coating on a silicon wafer at 6000 rpm for 1 minute. The dielectric layer with thickness of 20 µm was prepared by directly spinning PDMS (10:1) at 3000 rpm for 1 minute. The dielectric layer with thickness of 200 µm was obtained by PDMS spin coating (10:1) at 400 rpm for 10 seconds. For the dielectric layer with thickness of 2000 µm, PDMS (10:1) was poured into a mold with dimensions of 1 cm × 1 cm × 2000 µm (length × width × height). All PDMS-coated samples were subsequently cured in an oven at 70 °C for 2 hours, then cut into 1 cm × 1 cm squares and laminated onto laser-cut copper electrodes for assembly.

2.1.3. Sensing materials (PNC) characterization

PNC samples were cut into 10 × 10 mm^2 squares using a metal cutter. Electrical characterization of the PNC samples was performed by a series of carefully controlled measurements. First, a 10 × 10 mm^2 PNC sample was placed on a copper bottom electrode of the same size. This assembly was mounted onto a Dynamic Mechanical Analyzer (DMA; RSA-G2, TA Instruments), where a copper electrode attached to the DMA head served as the top electrode. The DMA was used to apply and measure pressure and displacement during the testing. The magnitude of impedance $|Z|$, phase angle θ, parallel capacitance C_{p} and parallel resistance R_{p} of the PNC samples (0%, 0.2%, 0.4%, 0.6%, and 0.8% CNT doping) were measured *in situ* using an LCR meter (3532-50, Hioki) at 1 kHz with a 2 V AC excitation voltage in parallel mode. The loss angle δ was calculated from the phase angle θ measured from the LCR meter. This fixed frequency and voltage were also used for the compression characterization of CPS to minimize any frequency-dependent effects (Li et al., 2022). The corresponding experimental schematics are shown in Fig. 5a. In a separate set of measurements to investigate the frequency effect, the same PNC samples were placed between the same electrode setup with the applied pressure fixed at 1 kPa, thus minimizing any compression-dependent effects. The excitation frequency was swept from 100 Hz to 100 kHz. During this frequency sweep, $|Z|$, θ, C_{p}, and R_{p} were again measured using the same set of LCR meters.

2.1.4. CPS characterization

The CPS characterization setup was analogous to that used for the PNC characterization. A $10 \times 10\,\mathrm{mm}^2$ PNC sample was placed atop a dielectric layer with different thicknesses (2 µm, 20 µm, 200 µm, 2000 µm) to systematically vary the capacitance ratio $C_{\mathrm{i}}/C_{\mathrm{p}}$. The dielectric layer was laminated onto a copper bottom electrode of the same size. This assembly was mounted onto a Dynamic Mechanical Analyzer (DMA; RSA-G2, TA Instruments), with a copper electrode attached to the DMA head serving as the top electrode. During compression testing, the magnitude of impedance $|Z|$, phase angle θ, sensor capacitance C_{s}, and resistance R_{s} was measured *in situ* in serial mode using the same LCR meter (3532-50, Hioki). It should be noted that our sensor operates as a leaky capacitor positioned on top of the dielectric layer; therefore, the *series mode* is the appropriate configuration for capacitance measurement. In this mode, the series capacitance C_{s} corresponds directly to the output capacitance of the sensor. The corresponding experiment schematics are shown in Fig. 6a. The loss angle δ was calculated from the phase angle θ measured with an LCR meter. The AC excitation frequency was fixed during each test at one of four values: 300 Hz, 1 kHz, 10 kHz, or 100 kHz.

2.2. Theoretical framework

To establish the coupling between mechanical deformation and electrical response in soft capacitive pressure sensors, we develop a general electromechanical framework linking stress, strain, porosity evolution, effective electrical properties, and the equivalent circuit representation of the device. Within this framework, the key component—the soft porous sensing layer—is first modeled. In principle, its mechanical behavior can be described by nonlinear constitutive laws, while the evolution of its effective electrical properties is governed by strain-dependent porosity, together with piezoresistive and piezocapacitive relations. These coupled relations are subsequently incorporated into an equivalent circuit model to describe the overall response of the assembled sensor. However, to derive a tractable analytical expression for sensitivity suitable for practical applications, several simplifying assumptions are introduced. These approximations allow us to capture the dominant mechanisms governing the sensing response while avoiding unnecessary model complexity.

Furthermore, it is worth noting that the proposed framework is not restricted to porous structures. Provided that appropriate models describing stress–strain behavior, porosity (and contact) evolution, and effective electrical properties are available, the same framework can be extended to other soft capacitive pressure sensor architectures, such as microdome or textile-based structures. In such cases, corresponding analytical expressions for sensitivity can be derived following the same methodology.

2.2.1. Constitutive law

We start by considering a general isotropic hyperelastic model described by a strain energy density function:

$$\Psi = W(\lambda_1, \lambda_2, \lambda_3) \tag{2}$$

where λ_1, λ_2, and λ_3 are the principal stretches, and $J = \lambda_1\lambda_2\lambda_3$ is the volume ratio.The corresponding Cauchy stress in the principal directions can be expressed as:

$$\sigma_j = J^{-1}\lambda_j \frac{\partial \Psi}{\partial \lambda_j} \tag{3}$$

which captures the nonlinear stress–strain behavior arising from large deformation and material compressibility. For capacitive pressure sensors, compressive loading is the primary mode of operation. Therefore, we focus on the principal direction $j = 1$, corresponding to the compression direction. The incremental stiffness (tangent modulus) along this direction can be written as:

$$\frac{\partial \sigma_1}{\partial \lambda_1} = \sum_{i=1}^{N} q(\mu_i, \lambda_1, \alpha_i, \beta_i, J), \tag{4}$$

where $q(\cdot)$ represents the nonlinear dependence on stretch and material parameters. However, for the purpose of deriving a simplified sensitivity model, and noting that the sensor operation is primarily governed by the low-pressure (small-strain) regime, the constitutive behavior is approximated using a linear elastic relation:

$$\frac{\partial \sigma_1}{\partial \lambda_1} \approx \frac{\partial P}{\partial \varepsilon} = E, \tag{5}$$

where P is the compressive stress, ε is the compressive strain, and E is the effective Young's modulus of the porous composite. This approximation enables a simple and physically transparent formulation for sensitivity analysis. Deviations from linearity at larger strains (e.g., plateau and densification regimes) are not expected to alter the fundamental scaling of sensitivity and will be considered in future work.

2.2.2. Porosity-strain relation

The porous structure can be characterized by its porosity ϕ, defined as the volume fraction of air within the material. Under compressive deformation, the pore volume decreases, leading to a strain-dependent evolution of porosity. In general, the change in volume of PNC is purely a result of change in air volume due to the incompressibility of the elastomeric materials. Therefore, the porosity can be found by:

$$\phi(\lambda_1, \lambda_2, \lambda_3) = 1 - \frac{1 - \phi_0}{\lambda_1\lambda_2\lambda_3}, \tag{6}$$

where λ_2 and λ_3 are principal stretches in the in-plane direction that can be found via stress-free conditions:

$$\sigma_2 = \frac{1}{\lambda_1\lambda_3}\frac{\partial\Psi}{\partial\lambda_2} = 0, \quad \sigma_3 = \frac{1}{\lambda_1\lambda_2}\frac{\partial\Psi}{\partial\lambda_3} = 0 \tag{7}$$

Specifically, when the porous mateiral has a Poisson's ratio of 0 as observed in our previous work, the equation can be reduced to:

$$\phi = 1 - \frac{1-\phi_0}{1-\varepsilon}, \tag{8}$$

2.2.3. Piezoresistive and piezocapacitive relation

The electrical response of the system arises from both capacitive and resistive contributions, which are coupled to mechanical deformation through changes in porosity, geometry, and microstructure. For stochastic soft porous sensing layers, rigorous analytical expressions for piezocapacitive and piezoresistive behavior are generally limited. Therefore, simplified but physically meaningful models are adopted. The piezocapacitive behavior of the capacitive branch (C_p) can be described using a parallel-plate approximation (Wang et al., 2024):

$$C_\mathrm{p} = \frac{k\epsilon_0 A}{d}, \quad k = k_\mathrm{air}\phi + k_\mathrm{matrix}(1-\phi), \tag{9}$$

where k is the effective dielectric constant, A is the electrode area, d is the thickness of the sensing layer, and ϵ_0 is the vacuum permittivity. Under compression, both the reduction in d and the increase in k (due to decreasing porosity) contribute to an increase in capacitance. The piezoresistive behavior of the resistive branch (R_p) is modeled using a modified form of Archie's law (Wang et al., 2024):

$$R_\mathrm{p} = R_{\mathrm{p},0}(1-\varepsilon)^n, \tag{10}$$

where $R_{\mathrm{p},0}$ is the resistance in the undeformed state, ε is the compressive strain, and n is an empirical exponent describing the sensitivity of conductivity to structural evolution. As porosity decreases under compression, conductive pathways become increasingly connected, resulting in enhanced conductivity (or reduced resistance). Together, these relations establish a direct coupling between strain, porosity, and electrical response, providing a simplified yet physically consistent framework for interpreting both piezocapacitive and piezoresistive behaviors. It is worth noting that the above expressions represent the simplest form of electromechanical coupling for stochastic porous systems. For other types of soft sensing layers with more regular or engineered structures (e.g., microdome or textile-based architectures), more refined models describing effective dielectric and conductive properties may be available. In such cases, the corresponding piezocapacitive and piezoresistive relations can be directly incorporated into the same framework, leading to similar analytical formulations for sensitivity.

2.2.4. Equivalent circuit models

This section presents the equivalent circuit models for the three CPS types. We begin with the double-branch model, originally developed for HRPS (Fig. 2(e)(ii)) and applicable for all three types. We then introduce single branch models for CPS with engineered dielectrics and engineered electrodes, both of which can be regarded as special cases of the double-branch framework.

2.2.5. *Double-branch model for hybrid response pressure sensor*

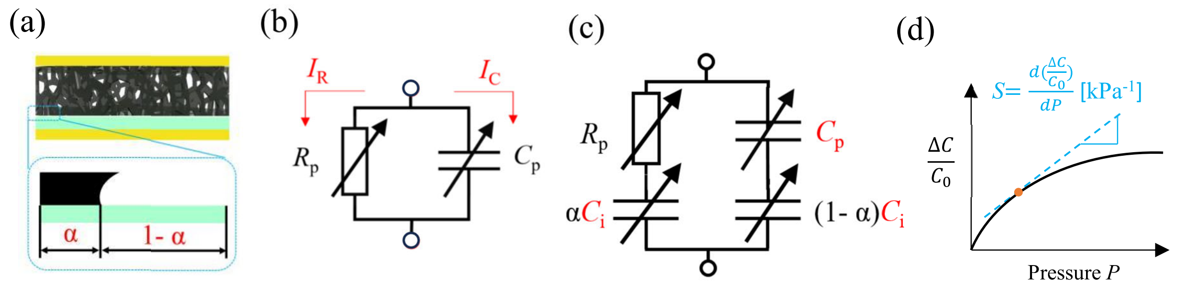

Figure 3: Physical interpretation of the model parameters. (a) The contact ratio α denotes the areal fraction of the dielectric layer that is in direct contact with the solid phase of the PNC. (b) The dielectric loss of the PNC, $\tan\delta$, reflects the ratio of the current flowing through the capacitive branch, I_{C}, to that through the resistive branch, I_{R}. (c) Schematic illustration of the capacitance ratio $C_{\mathrm{i}}/C_{\mathrm{p}}$. (d) The sensitivity S is defined as the slope of the relative capacitance change with respect to the applied pressure.

Before delving into the mathematical details, we first introduce the key dimensionless parameters and their physical interpretations for HRPS. Figure 3a shows a magnified view of CPS at the interface between the porous nanocomposites and the dielectric layer, highlighted by the cyan box. In this configuration, part of the dielectric layer is in direct contact with the nanocomposite while the remainder is exposed to air. When there is a significant discrepancy between the electrical properties of the nanocomposite and the air, the top surface of the dielectric layer is no longer equipotential (Ha et al., 2024), requiring separate treatment of the two regions. We define the contact ratio $\alpha \in [0,1]$ as the fraction of the area where the surface of the dielectric layer is in direct contact with the nanocomposite. Accordingly, the fraction of the area in direct contact with air is $1-\alpha$. As direct measurement of the contact ratio is difficult, we approximate α with the porosity of the PNC ϕ through following expression:

$$\alpha = 1 - \phi. \tag{11}$$

Equation 11 adopts a simplified representation that does not fully capture the complex deformation, buckling, and collapsing of the ligmaents in the PNC. However, as will be discussed in later section, the model predictions are relatively insensitive to the specific value of α across most cases considered. Therefore, this simplification does not materially affect the key conclusions of this work. In this work, we fix the initial porosity of the sensing layer at $\phi_0 = 0.86$, which yields an initial contact ratio of $\alpha_0 = 0.14$. The contact ratio α naturally depends on the deformation: as the pressure increases, more nanocomposites come into contact with the dielectric layer.

Figure 3b illustrates the equivalent circuit of the porous nanocomposite measured between two electrodes. The circuit consists of a parallel resistance R_{p} and capacitance C_{p}. The total current divides between the resistive branch (I_{R}) and the capacitive branch (I_{C}), and their ratio relates to the phase angle θ (loss angle

δ) through the impedance relationship:

$$|\tan\theta| = \left|\frac{I_{\mathrm{C}}}{I_{\mathrm{R}}}\right| = \omega R_{\mathrm{p}} C_{\mathrm{p}}, \quad \tan\delta = \left|\frac{I_{\mathrm{R}}}{I_{\mathrm{C}}}\right| = \frac{1}{\omega R_{\mathrm{p}} C_{\mathrm{p}}} = \left|\frac{1}{tan\ \theta}\right| \tag{12}$$

where ω denotes angular frequency of the excitation AC signal.

Figure 3c presents the full equivalent circuit of the hybrid response pressure sensor. Based on the definition of contact ratio α, the dielectric layer is divided into two capacitive branches: $C_{\mathrm{il1}} = \alpha C_{\mathrm{i}}$, which contacts the PNC directly, and $C_{\mathrm{il2}} = (1-\alpha)C_{\mathrm{i}}$, which interfaces with air. We highlight two key capacitive elements in red: the total capacitance of flat dielectric layer C_{i} and the parallel capacitance of the nanocomposite C_{p}. Their ratio, defined as the capacitance ratio $C_{\mathrm{i}}/C_{\mathrm{p}}$, is a dimensionless number that quantifies the relative contribution of the dielectric layer to the overall electrical response. $C_{\mathrm{i}}/C_{\mathrm{p}} \approx 1$ indicates comparable contributions from the two layers, while a large ratio suggests that the contribution of PNC to total impedance is dominant. The influence of this ratio on sensor performance will be discussed in section 3. The capacitance of the circuit model for the hybrid response pressure sensor can therefore be expressed in terms of the parameters introduced above.

$$C_{\mathrm{CPS}} = C_{\mathrm{i}} \frac{\left(1 + \frac{C_{\mathrm{p}}}{(1-\alpha)C_{\mathrm{i}}} + \frac{C_{\mathrm{p}}}{\alpha C_{\mathrm{i}}}\right)^2 \tan^2\delta + 1}{\left(1 + \frac{C_{\mathrm{p}}}{(1-\alpha)C_{\mathrm{i}}} + \frac{C_{\mathrm{p}}}{\alpha C_{\mathrm{i}}}\right)\left(\frac{1}{\alpha} + \frac{C_{\mathrm{p}}}{\alpha(1-\alpha)C_{\mathrm{i}}}\right)\tan^2\delta + \frac{C_{\mathrm{i}}}{C_{\mathrm{p}}} + \frac{1}{1-\alpha}}, \tag{13}$$

A typical normalized capacitance response of a CPS is shown in Fig. 3d, where $\Delta C = C - C_0$ is the change in capacitance under applied pressure P, and C_0 is the initial capacitance. The sensitivity S of the CPS is defined as the slope of the curve at a given point (highlighted in orange):

$$S = \frac{d\left(\Delta C/C_0\right)}{dP}, \tag{14}$$

By substituting Eq. 13 into the sensitivity definition in Eq. 14, we arrive at the closed-form expression below (with the full derivation provided in Appendix B.4). This result is identical to the expression given in Eq. B.37:

$$S = \frac{\partial(\frac{\triangle C}{C_0})}{\partial P} = \frac{\partial(\frac{\triangle C}{C_0})}{\partial C_{\mathrm{p}}}\frac{\partial C_{\mathrm{p}}}{\partial\phi}\frac{\partial\phi}{\partial\epsilon}\frac{\partial\epsilon}{\partial P} + \frac{\partial(\frac{\triangle C}{C_0})}{\partial\tan\delta}\frac{\partial\tan\delta}{\partial\phi}\frac{\partial\phi}{\partial\epsilon}\frac{\partial\epsilon}{\partial P} + \frac{\partial(\frac{\triangle C}{C_0})}{\partial\alpha}\frac{\partial\alpha}{\partial\phi}\frac{\partial\phi}{\partial\epsilon}\frac{\partial\epsilon}{\partial P} = f(E, \tan\ \delta, \frac{C_{\mathrm{i}}}{C_{\mathrm{p}}}, \alpha, n), \tag{15}$$

For simplicity, we consider a simple linear constitutive law described by the following energy density function:

$$\Psi = \frac{E}{2}\left[(\lambda_1 - 1)^2 + (\lambda_2 - 1)^2 + (\lambda_3 - 1)^2\right] \tag{16}$$

Notice that the energy density function results in a Poisson's ratio of 0, consistent with our earlier studies (Wang et al., 2024).

This simple constitutive law gives us the following sensitivity when $P = 0$:

$$\begin{aligned} f = \frac{1}{E}\Bigg[& \frac{\left(\frac{1}{\alpha} + \frac{C_\mathrm{p}}{\alpha(1-\alpha)C_\mathrm{i}}\right)\left(\frac{C_\mathrm{p}}{C_\mathrm{i}}\frac{-1}{(1-\alpha)^2}\right)\cdot\tan^2\delta + \left[\frac{2(n-1)}{1-\alpha} - \frac{\alpha}{(1-\alpha)^2} + (2n-1)\frac{C_\mathrm{i}}{C_\mathrm{p}}\right]}{(\frac{C_\mathrm{p}}{\alpha C_\mathrm{i}} + \frac{C_\mathrm{p}}{(1-\alpha)C_\mathrm{i}} + 1)(\frac{1}{\alpha} + \frac{C_\mathrm{p}}{(1-\alpha)\alpha C_\mathrm{i}})\cdot\tan^2\delta + (\frac{C_\mathrm{i}}{C_\mathrm{p}} + \frac{1}{1-\alpha})} + \\ & \frac{2\frac{C_\mathrm{p}}{(1-\alpha)^2 C_\mathrm{i}}(\frac{C_\mathrm{p}}{\alpha C_\mathrm{i}} + \frac{C_\mathrm{p}}{(1-\alpha)C_\mathrm{i}} + 1)\cdot\tan^2\delta - 2(n-1)}{(\frac{C_\mathrm{p}}{\alpha C_\mathrm{i}} + \frac{C_\mathrm{p}}{(1-\alpha)C_\mathrm{i}} + 1)^2\cdot\tan^2\delta + 1}\Bigg], \end{aligned} \tag{17}$$

where E is the Young's modulus of the sensing material, n is the exponent of Archie's law, $\tan\delta$ is the tangent loss or dielectric loss, C_p is the parallel capacitance of the sensing layer and C_i is the parallel capacitance of the dielectric layer. The sensitivity S (units: kPa^{-1}) can thus be expressed entirely in terms of the intrinsic properties of the sensing material.

2.2.6. Single-branch model for CPS with engineered dielectrics

When the sensing layer is undoped or only lightly doped, its loss angle remains close to 0°, and the contribution of the resistive branch can be neglected. In this case, the electromechanical response can be captured by a simplified model in which C_p and C_i are connected in series (Fig. 2(d)(ii)), with the total capacitance given by:

$$C_\mathrm{CPS} = \frac{C_\mathrm{p}C_\mathrm{i}}{C_\mathrm{p} + C_\mathrm{i}}, \tag{18}$$

and the sensitivity at small pressure is obtained as follows:

$$S = \left.\frac{\partial(\frac{\triangle C}{C_0})}{\partial P}\right|_{P=0} = \frac{1}{E}\frac{\frac{C_\mathrm{i}}{C_\mathrm{p0}}}{1 + \frac{C_\mathrm{i}}{C_\mathrm{p0}}} = \frac{1}{E}\frac{\frac{C_\mathrm{i}}{C_\mathrm{p}}}{1 + \frac{C_\mathrm{i}}{C_\mathrm{p}}}, \tag{19}$$

2.2.7. Single-branch model for CPS with engineered electrodes

Engineered electrodes represent the other limiting case, where the current flow through the capacitance branch is negligible compared to that through the resistive branch. In this case, as we mentioned in Appendix A, the interfacial effects are dominating; therefore, the double-branch model reduces to a serial connection of sensing layer resistance and dielectric layer capacitance (Fig. 2(f)(ii)). The total capacitance of the sensor output C_CPS is given by:

$$C_\mathrm{CPS} = \alpha C_\mathrm{i}, \tag{20}$$

The normalized capacitance and sensitivity under small pressure can be written as follows:

$$\frac{\triangle C}{C_0} = \frac{\alpha}{\alpha_0} - 1, \tag{21}$$

$$S = \left.\frac{\partial(\frac{\triangle C}{C_0})}{\partial P}\right|_{P=0} = \frac{1}{\alpha_0}\left.\frac{\partial\alpha}{\partial P}\right|_{P=0} = \frac{1}{E}, \tag{22}$$

where α_0 is the initial contact ratio and α is the current contact ratio.

3. Results and discussions

3.1. Comparisons between circuit models and the boundary between three CPS types

To demonstrate the generality of the double-branch model and investigate the boundaries between the three types of CPS, we plot in Fig. 4 the predicted sensitivity of the three models presented in the previous section. The horizontal axis represents the loss tangent $\tan\delta$, and the vertical axis represents the pressure sensitivity S in the unit of kPa^{-1}. The following parameters, representative of our system, are used in all cases: Young's modulus of the sensing material $E = 2.18$ kPa, Archie's law coefficient $n = 4$, capacitance ratio $C_\mathrm{i}/C_\mathrm{p} = 1000$, and contact ratio $\alpha = 0.14$. The single-branch models for engineered dielectrics and engineered electrodes (Eqs. 19 and 22) are independent of $\tan\delta$ and therefore appear as horizontal solid cyan and red lines in the plot. In contrast, the double-branch model exhibits a non-monotonic dependence on $\tan\delta$ (green dashed line), first increasing and then decreasing. In the limit of small $\tan\delta$, where the sensing layer behaves nearly as a purely capacitive material, the double-branch model converges to the single-branch model for engineered dielectrics. Conversely, in the limit of large $\tan\delta$, where the sensing layer becomes nearly resistive, the double-branch model converges to the single-branch model for engineered electrodes. The convergence to the two single-branch models occurs when the following threshold conditions are satisfied:

$$\text{Engineered Dielectric Limit:}\quad \tan\delta < \frac{1}{\sqrt{\frac{C_\mathrm{i}}{C_\mathrm{p}}}}\sqrt{\frac{2\alpha}{(1-\alpha)n}}, \tag{23}$$

$$\text{Engineered Electrode Limit :}\ \tan\delta > \frac{C_\mathrm{i}}{C_\mathrm{p}}\sqrt{\frac{n\alpha}{4(1-\alpha)}}, \tag{24}$$

which are shown as the left and right dashed boundaries in Fig. 4 and divide the plot into three regimes.

As shown earlier, the single-branch models can be regarded as limiting cases of the double-branch model. Therefore, we focus on the double-branch model in the following sections. The double branch model involves 5 parameters (Eq. 15): Young's Modulus E, loss angle δ (or $\tan\delta$), capacitance ratio $C_\mathrm{i}/C_\mathrm{p}$, contact ratio α, and Archie's law coefficient n. The contact ratio α is considered as a fixed structural parameter independent of the properties of the constituent material, as discussed earlier, while the effect of the other parameters will be studied systematically using a combined experimental and theoretical approach in the following sections.

3.2. Effects of doping ratio

In this section, we examine how the doping ratio influences the intrinsic electromechanical properties of PNC and, in turn, the sensitivity of the corresponding CPS devices. Because the doping ratio simultaneously modulates the loss angle δ, the capacitance ratio $C_\mathrm{i}/C_\mathrm{p}$, and the exponent coefficient in Archie's law n, it provides an effective means to evaluate the proposed double-branch model over a wide range of material behaviors. To obtain the required model inputs, we first quantify how these model parameters evolve with doping by characterizing the electromechanical properties of the porous nanocomposites (PNC). We then independently characterize CPS devices assembled from the same PNCs and compare their measured

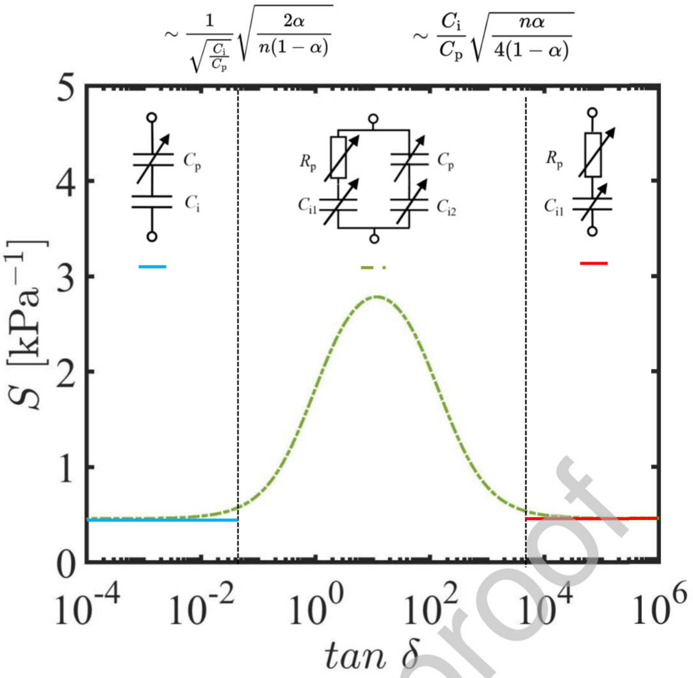

Figure 4: The sensitivity in the double-branch model (green dashed line) first increases and then decreases with the loss tangent, asymptotically approaching the equivalent-circuit model of CPS with engineered dielectrics (blue solid horizontal line) in the small–loss-tangent limit and that of CPS with engineered electrodes (red solid horizontal line) in the large–loss-tangent limit. Approximate boundaries between the sensor types are identified and indicated by black dashed lines.

sensitivities with theoretical predictions. For each doping ratio, three samples were prepared and tested to ensure repeatability, and the averaged properties were used for model validation (raw data in supplementary figure 1 and supplementary table 1).

Figure 5a illustrates the experimental setup used for the electromechanical characterization of porous nanocomposites (PNC) without a dielectric layer. The characterization procedure follows those described in the methods section. The four key parameters, Young's modulus E, parallel capacitance C_p, loss angle δ (or $\tan\delta$), and Archie's law exponent n, were evaluated at a reference pressure of 1 kPa, which will be marked by hollow circles in subsequent figures. This reference pressure was selected for two reasons. First, 1 kPa represents the minimal pressure relevant for physical human–robot interaction (Zang et al., 2015). Second, the loss angle becomes noisy near zero pressure due to variations in the contact state of the PNC.

Figure 5b summarizes the dependence of the extracted parameters on the doping ratio. For clarity of presentation, a representative specimen from each doping level is shown in Figure 5b to demonstrate how the measured PNC properties are used to predict the corresponding CPS sensitivity. Figure 5b(i) shows the relationship between compressive strain ϵ_1 and applied pressure (0%: red, 0.2%: orange, 0.4%: green, 0.6%: blue, 0.8%: purple). All doping ratios exhibit a characteristic nonlinear J-shape typical of soft porous materials. In the low-strain regime (inset), the response is nearly linear, and the curves collapse onto

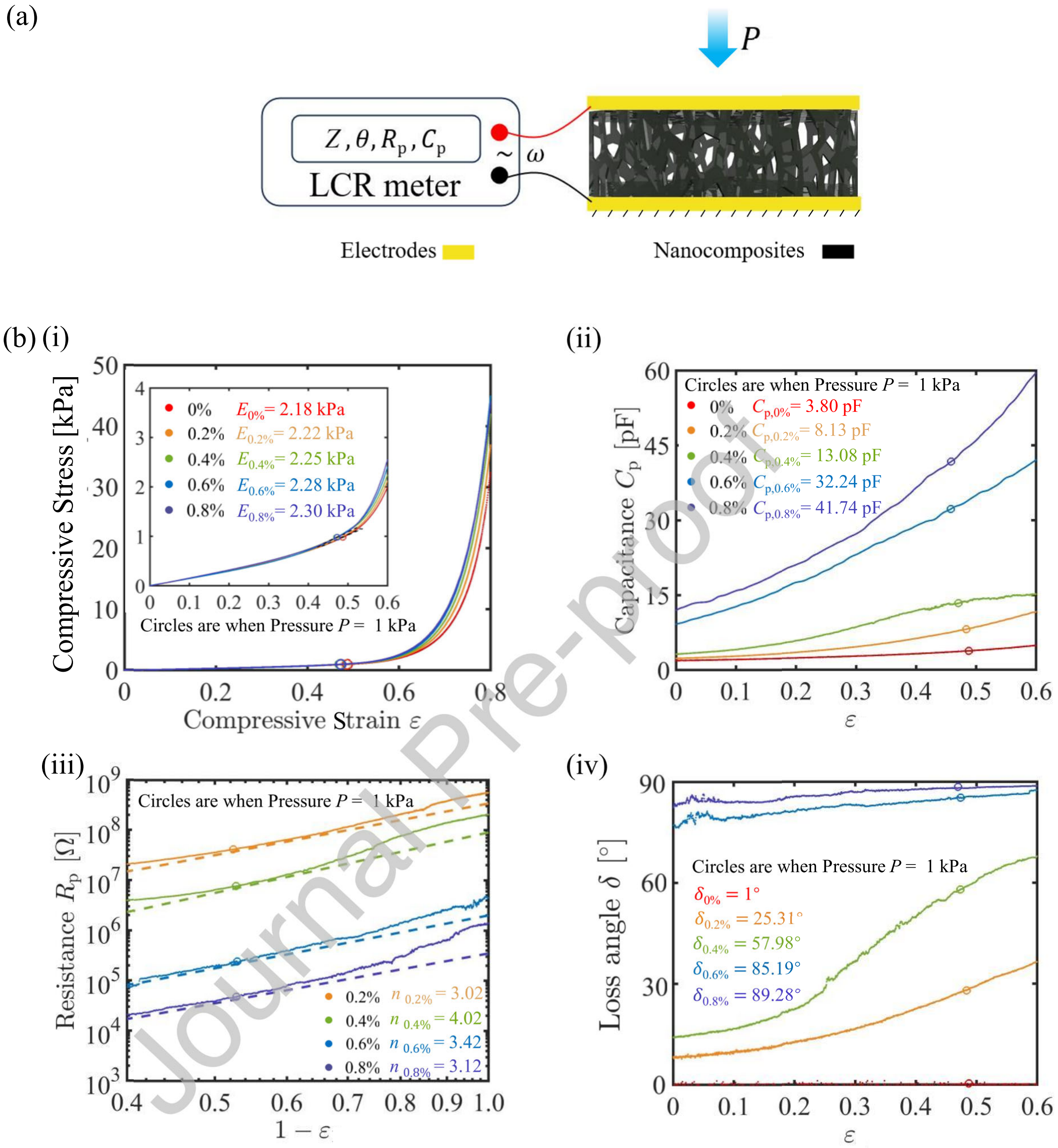

Figure 5: (a) Schematic of the measurement setup, where an LCR meter applies an AC excitation (frequency ω) and records electro-mechanical characterization of a porous nanocomposites without dielectric layer for measuring $E, C_{\mathrm{p}}, n, \delta$ at 1 kPa pressure. (b) Strain-dependent electromechanical responses of PNCs with varying CNT doping ratios. (i) Compressive stress versus strain, showing similar nonlinear stiffening behavior across all doping ratios and nearly identical initial linear elastic responses (inset). (ii) Parallel capacitance C_{p} increases with compressive strain, where higher CNT doping leads a larger effective permittivity and therefore higher capacitance. (iii) Parallel resistance R_{p} increases with 1-ϵ, where increasing CNT doping dramatically reduces R_{p} and enhances piezoresistivity. The exponent in Archie's law n is shown in the legend. (iv) Loss angle δ vs. compressive strain, undoped samples behave nearly as ideal dielectrics ($\delta \approx 1°$), while higher CNT contents yield progressively larger δ, approaching conductive behavior as δ approaches 90°.

each other. The tangent moduli evaluated using pressure points at 1 ± 0.05 kPa yield $E_{0\%} = 2.18\,\mathrm{kPa}$, $E_{0.2\%} = 2.22\,\mathrm{kPa}$, $E_{0.4\%} = 2.25\,\mathrm{kPa}$, $E_{0.6\%} = 2.28\,\mathrm{kPa}$, and $E_{0.8\%} = 2.30\,\mathrm{kPa}$. Figure 5b(ii) displays the parallel capacitance C_p of the PNC as a function of compressive strain.The reference capacitance at 1 kPa increases monotonically with the doping ratio from $C_{\mathrm{p},0\%} = 3.80\,\mathrm{pF}$ to and $C_{\mathrm{p},0.8\%} = 41.74\,\mathrm{pF}$. Figure 5b(iii) shows the parallel resistance R_p plotted against $1 - \varepsilon$, from which Archie's law exponents n were extracted to be: $n_{0.2\%} = 3.42$, $n_{0.4\%} = 4.52$, $n_{0.6\%} = 3.42$, and $n_{0.8\%} = 3.12$. The 0% is purely capacitive, so n was not defined. Figure 5b(iv) presents the loss angle δ as a function of compressive strain. The values of δ at reference pressure 1 kPa increase rapidly with doping ratio from $\delta_{0\%} = 1°$ to $\delta_{0.8\%} = 89.28°$, confirming a transition from capacitive to resistive behavior as the CNT doping increases. Finally, the capacitance of the dielectric layer capacitance C_i was calculated to be 1.195 nF based on the thickness of 2 μm and the dielectric constant of 2.3 for the dielectric layer. Using the extracted parameters $(E, \delta, C_\mathrm{i}/C_\mathrm{p}, n, \alpha)$, the sensitivity of each CPS is calculated based on the double-branch model, which is summarized in Table 2.

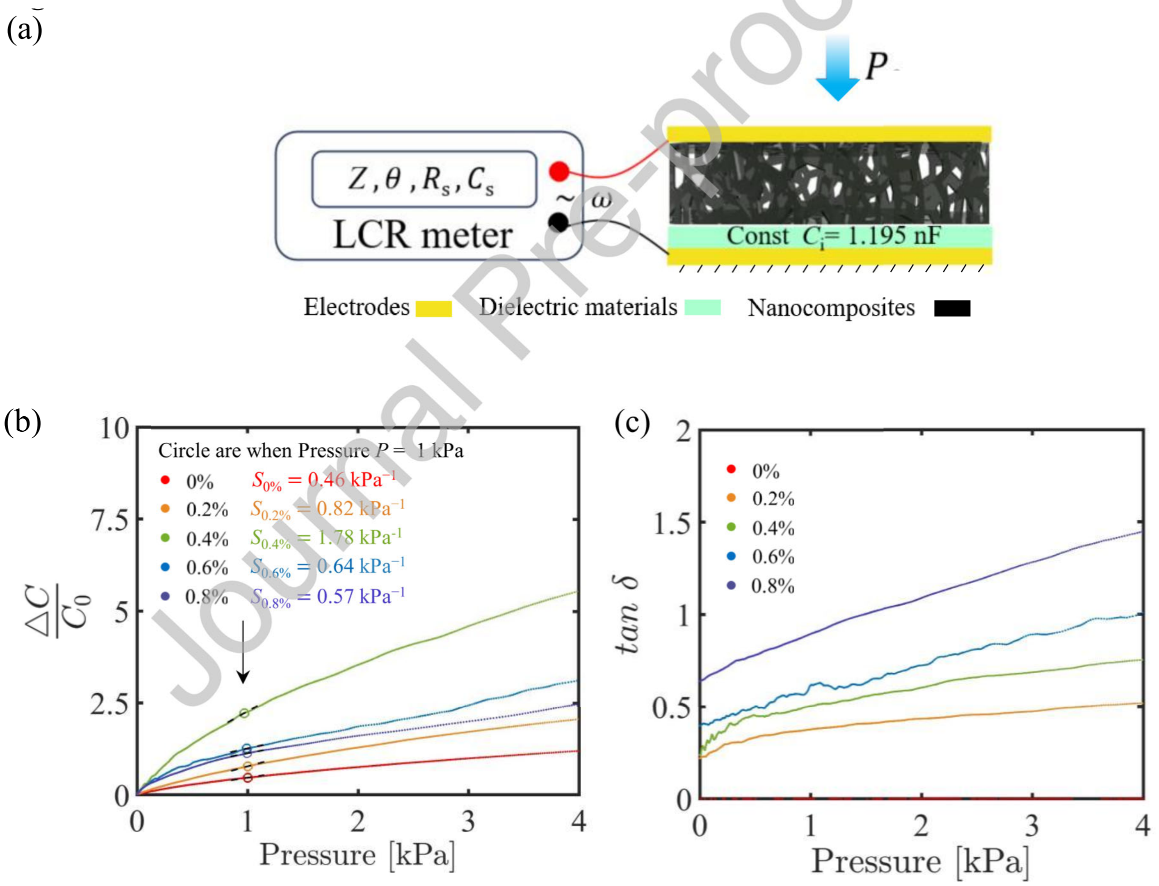

Figure 6: (a) Schematic of the experimental setup. An LCR meter applies an AC excitation (frequency ω) and records impedance Z, phase angle θ, the serial resistance R_s, and the serial capacitance C_s of the CPS; (b) Pressure vs. $\triangle C/C_0$ with sensitivity values at 1 kPa ($S = \mathrm{d}(C/C_0)/\mathrm{d}P|_{P=1\ \mathrm{kPa}}$) highlighted for each doping ratio, showing a clear nonmonotonic trend; (c) Pressure vs. dielectric loss $\tan\delta$ of sensors with various doping ratio. Higher doping ratio results in higher dielectric loss.

To validate the predicted sensitivity, we conducted an electromechanical characterization of CPS devices assembled using the same PNC batches characterized in the previous section. As shown in Figure 6a, a fixed thickness dielectric layer (2 µm) was laminated below each PNC to form a consistent sandwich structure. The characterization protocol follows the procedure described in the Methods section. The normalized capacitance change $\Delta C/C_0 = (C - C_0)/C_0$ shows a nonmonotonic trend, with 0.4% doping ratio showing the highest sensitivity of $S_{0.4\%} = 1.78$, which is consistent with the previous findings (Fig. 6b(i)) (Ha et al., 2021). The measured sensitivities are included in Table 2, showing good agreement with the prediction. Fig. 6c shows the evolution of the loss tangent ($\tan\delta$) as a function of applied pressure for different CNT doping ratios. At zero doping (0%), the loss tangent remains close to zero and is nearly pressure independent, indicating purely capacitive behavior. With an increasing doping ratio, $\tan\delta$ increases and exhibits a monotonic increase with pressure. This trend indicates that the sensor's response transitions from a simple capacitive mechanism to a hybrid mechanism. Here, pressure-induced deformation modulates the resistance and contact network within the PNC, causing the dissipative (resistive) component to grow relative to the storage (capacitive) component. This confirms that doping serves as a critical design parameter to shift the sensor into the hybrid response zone.

Doping ratio	δ	$\tan\delta$	n	E [kPa]	$\frac{C_i}{C_p}$	α	Predicted S [kPa^{-1}]	Measured S [kPa^{-1}]
0%	1°	0.0175	NA	2.18	$\frac{1.195\ \mathrm{nF}}{3.80\ \mathrm{pF}}$	0.14	0.48	0.46
0.2%	25.31°	0.4729	3.02	2.22	$\frac{1.195\ nF}{8.13\ \mathrm{pF}}$	0.14	0.81	0.82
0.4%	57.98°	1.5991	4.02	2.25	$\frac{1.195\ nF}{13.08\ \mathrm{pF}}$	0.14	1.99	1.78
0.6%	85.19°	11.8838	3.42	2.28	$\frac{1.195\ nF}{32.24\ \mathrm{pF}}$	0.14	0.51	0.64
0.8%	89.28°	79.5733	3.12	2.30	$\frac{1.195\ nF}{41.74\ \mathrm{pF}}$	0.14	0.46	0.57

Table 2: Model parameters extracted from experiments for samples of various doping ratios at excitation frequency of 1 Hz and reference pressure of 1 kPa, including loss angle δ, loss tangent *tan* δ, Young's modulus E, parallel capacitance, C_{p}, exponent coefficient in Arichie's law n, contact ratio α, and sensitivity S.

To enable predictive sensor design, we next establish empirical relationships between the doping ratio t and the key variables $\tan\delta$, n, and $C_{\mathrm{i}}/C_{\mathrm{p}}$. As shown in Fig. 7a, the experimental data for $\tan\delta$ (dots) exhibit a rapid increase with increasing CNT doping ratio, consistent with enhanced conductivity and reduced capacitive dominance. A fitted exponential relation (dashed line) captures this trend well:

$$\tan\delta = 0.044\, e^{10.52t}. \tag{25}$$

Figure 7b illustrates how the exponent in Archie's law n varies non-monotonically with doping. n reflects the degree of piezoresistivity, which is maximized when mechanical deformation induces the largest change in the conductive network. This maxima takes place near the percolation threshold, as experimentally observed in previous work (Kang et al., 2009). The relation ship is interpolated by a third-order polynomial relation:

$$n = 23.54t^3 - 43.02t^2 + 23.25t - 0.008 \tag{26}$$

In Fig. 7c, the capacitance ratio $C_\mathrm{i}/C_\mathrm{p}$ exhibits rapid decay with increasing doping ratio, reflecting the increase in C_p with doping due to the enhanced permittivity of the nanocomposite. An exponential form was adopted to capture the trend:

$$\frac{C_\mathrm{i}}{C_\mathrm{p}} = 290\, e^{-3.11t} \tag{27}$$

The fitted expression allows continuous interpolation and extrapolation across doping levels, effectively bridging the material-level design variable (doping ratio) with the governing parameters of the double-branch model. Substituting Eqs. 25, 26, and 27 into the double-branch model Eq. 17, we are able to compute and predict the sensitivity of CPS as a function of the doping ratio, as shown in Fig. 8. The model predicts that the true optimum doping ratio is 0.34% with a sensitivity of 2.00 kPa^{-1}, showing a significant improvement of 15% compared to the previous best case, achieved by changing the doping ratio by only 0.06%.

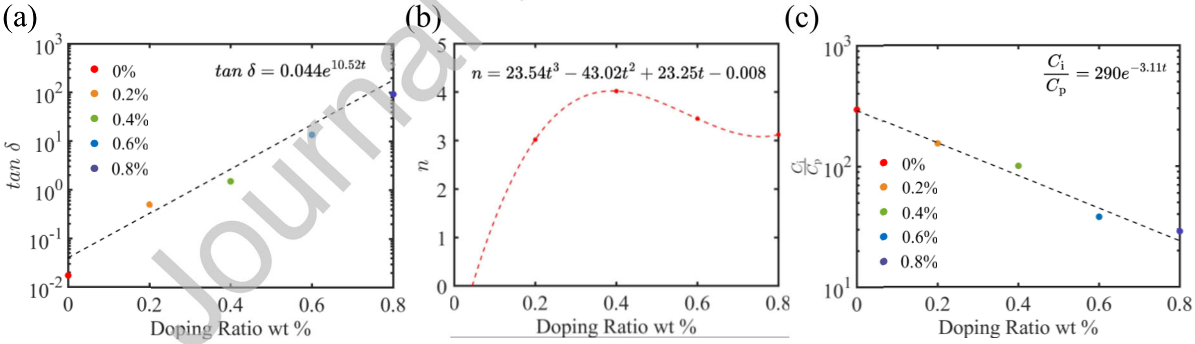

Figure 7: Analytical fitting of experimentally measured key model parameters as continuous functions of the CNT doping ratio t. (a) The loss tangent $\tan\delta$ increases exponentially with increasing doping ratio. (b) The exponential coefficient n in Archie's law exhibits a nonmonotonic dependence on doping ratio, first increasing and then decreasing, which is captured by a polynomial fit. (c) The capacitance ratio $C_\mathrm{i}/C_\mathrm{p}$ decreases exponentially with increasing doping ratio t.

To further validate this predictive capability, we fabricated a new batch of CPS using PNC with the optimal doping ratio predicted by the model of 0.34% and characterized its sensitivity. The measured sensitivity aligns closely with the theoretical prediction, providing strong evidence that the model can guide material design and optimization without exhaustive trial-and-error experimentation. In addition, Fig. 8

quantitatively captures the non-monotonic dependence of sensitivity on the doping ratio. This behavior is primarily attributed to the sharp increase in the loss tangent with increasing doping ratio (Fig. 7a), which drives the sensitivity to first rise and then fall (Fig. 4). Although the exponential coefficient in Archie's law n and the capacitance-competition ratio also vary with the doping ratio, their effects are comparatively minor compared to the loss tangent, as will be discussed in later sections. A similar non-monotonic sensitivity–doping relationship has been widely reported in previous studies (Ha et al., 2021, 2024; He et al., 2023; Zhong et al., 2023; Feng et al., 2023; Li et al., 2023; Qu et al., 2023; Luan et al., 2024; Shang et al., 2025; Zhao et al., 2025; Zheng et al., 2025; Xiao et al., 2026). Although many of these studies do not explicitly identify their devices as HRPS, the similarity in sensor design, i.e., doped composites in combination with an additional dielectric layer, together with the non-monotonic sensitivity–doping trend indicates the coexistence of resistive and capacitive contributions. From this perspective, such sensors can be interpreted as exhibiting HRPS behavior.It is also worth noting that the non-monotonic sensitivity–doping relationship is not unique to porous soft capacitive pressure sensors, but is also observed in micro-dome-based capacitive pressure sensors (Zhang et al., 2025). This cross-structural consistency further supports the generality of the proposed theoretical framework.

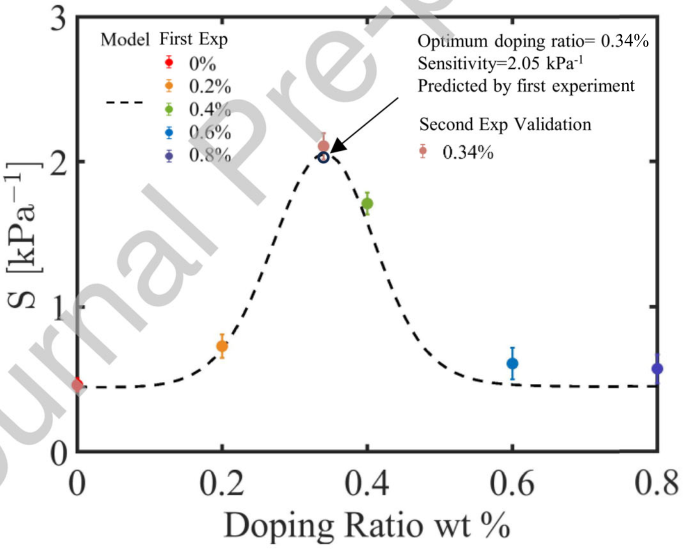

Figure 8: The model quantitatively captures the nonmonotonic dependence of initial sensitivity on doping ratio, with the sensitivity first increasing and then decreasing, and predicts an untested optimal doping ratio.

3.3. *Effects of excitation frequency*

In this section, we examine the effect of the excitation frequency—a conveniently tunable experimental parameter that does not require modifying the sensor yet can significantly influence the performance of CPS (Li et al., 2022). Since the loss angle δ varies with both the doping ratio and the frequency, we isolated the frequency effect by fixing the applied pressure at 1 kPa and placing the PNC samples between two copper electrodes. Then we perform the frequency sweep from 100 Hz to 100 kHz and measure the key electrical parameters *in situ*.

Figure 9a shows that parallel resistance R_p decreases monotonically with increasing frequency, consistent with capacitive dominance at higher frequencies. Figure 9b shows that the parallel capacitance C_p also decreases with increasing frequency, but in a much smaller rate. As the capacitance of the dielectric layer $C_\mathrm{i} = 1.195\,\mathrm{nF}$ is constant, the calculated capacitance rival ratio $C_\mathrm{i}/C_\mathrm{p}$ (Fig. 9c) increases with increasing frequency. Figure 9d shows the frequency dependence of tan δ, the key governing parameter in the double-branch model. In particular, tan δ decreases with increasing frequency, suggesting a shift from resistive to capacitive behavior with increasing frequency. The Archie's coefficient n was found to be independent of excitation frequency (Supplementary figure 4).

The resistance–frequency relationship of porous nanocomposites (PNC) can be approximated by the following empirical expression (Barrau et al., 2003; Li et al., 2022):

$$\frac{R_\mathrm{p}(f)}{R_\mathrm{p0}} = \frac{\sigma_\mathrm{dc}}{\sigma_\mathrm{dc} + \beta(2\pi f)^s}, \tag{28}$$

where R_p is the parallel resistance, f the excitation frequency applied to the CPS, σ_dc is the direct-current conductivity of the PNC, and β and s are fitting constants. Similarly, the capacitance–frequency relationship of the PNC can be expressed as (Barrau et al., 2003; Li et al., 2022):

$$C_\mathrm{p}(f) = \frac{(k_0 + \gamma(2\pi f)^{-q})\epsilon_0 A}{d}, \tag{29}$$

where C_p is the parallel capacitance, k_0 is the low-frequency dielectric constant, ϵ_0 is the vacuum permittivity, A is the electrode area, d is the thickness of the dielectric layer, and γ and q are fitting constants. The fitted σ_dc, β, γ and q are listed in Table 3:

Doping ratio	σ_dc [s/m]	β	s	k_0	γ	q
0.2 wt %	2e-13	2.51e-14	0.75	1.15	38.26	-0.15
0.4 wt %	7e-9	1.19e-10	0.72	1.69	92.6	-0.23
0.6 wt %	1.6e-6	2.12e-7	0.65	2.11	396	-0.27
0.8 wt %	4e-5	1.39e-9	0.69	4.51	637	-0.29

Table 3: Fitting parameters (σ_dc, β, k_0, γ and q) used to model the frequency-dependent behaviors of parallel resistance R_p and parallel capacitance C_p of porous nanocomposites (PNC).

Using the phenomenological models for frequency dependent C_p, $\tan\delta$, and $C_\mathrm{i}/C_\mathrm{p}$, we can now apply the double-branch model to predict the sensitivity as a function of the excitation frequency for all doping ratios within a frequency range between 100 Hz to 1 MHz (Fig. 10). This enables optimization of CPS performance by tuning the frequency. For each doping ratio, an optimal excitation frequency is identified as the frequency at which the predicted sensitivity of the model reaches its maximum. The optimal excitation frequency is found to be highly dependent on the doping ratio. For doping ratio of 0.2%, the sensitivity decrease monotonically with frequency, and the optimal excitation frequency is 100 Hz (Fig. 10a). For other doping ratios, the sensitivity exhibits a non-monotonic trend, with maxima at approximately 300 Hz, 1 MHz, and 538 kHz for doping ratio of 0.4%, 0.6%, and 0.8% respectively (Fig. 10b-d).

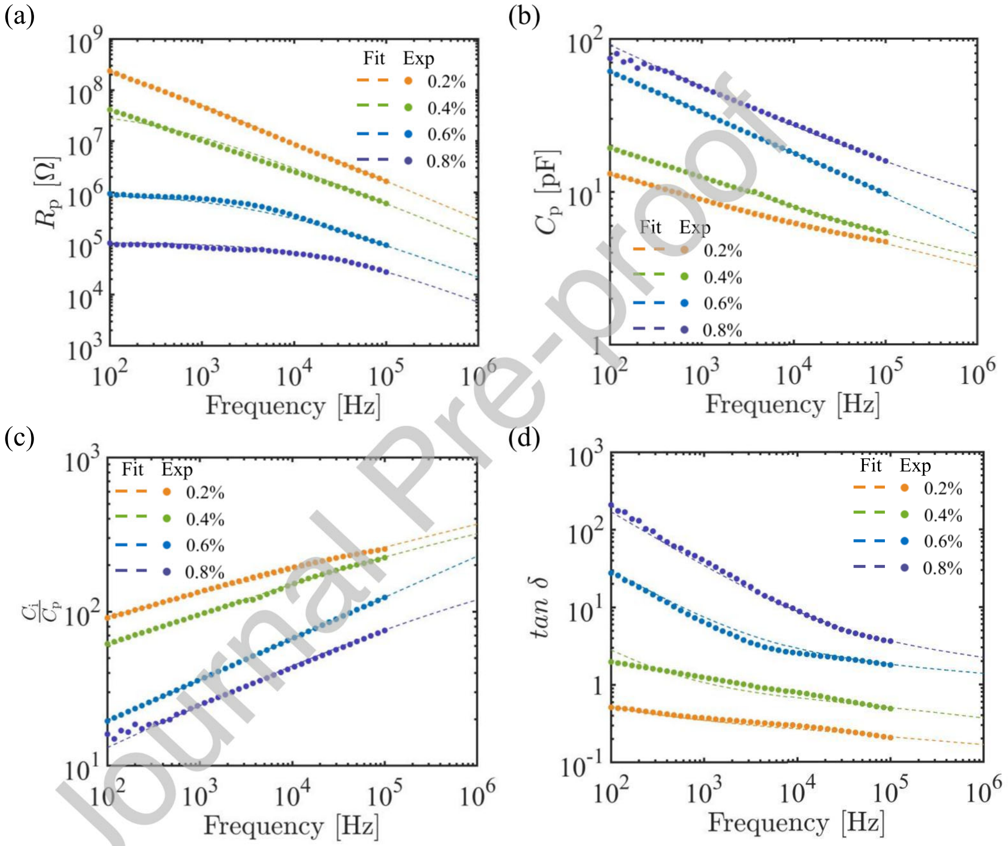

Figure 9: Frequency dependence of model parameters obtained from frequency-sweep measurements and corresponding fits for nanocomposites with various doping ratios. (a) Parallel resistance R_p decreases with increasing frequency. (b) Parallel capacitance C_p decreases with increasing frequency. (c) Capacitance ratio $C_\mathrm{i}/C_\mathrm{p}$ increases with increasing frequency. (d) Loss tangent $\tan\delta$ decreases with increasing frequency.

To experimentally validate these predictions, we conducted a second round of measurements for each doping ratio. In contrast to the previous characterization, where the pressure was fixed at 1 kPa to isolate the frequency effects, these measurements swept the applied pressure at discrete excitation frequencies of 300 Hz, 1 kHz, 10 kHz and 100 kHz. The measured sensitivities are shown as solid dots in Figure 10. Due to instrument bandwidth limitations, the optimal frequencies predicted by the model could not be experimentally accessed in some cases, particularly those above 100 kHz. However, the experimental trends closely follow the theoretical curves in the available frequency range, confirming the predictive capacity of the model and demonstrating that the excitation frequency provides a practical means to modulate CPS performance.

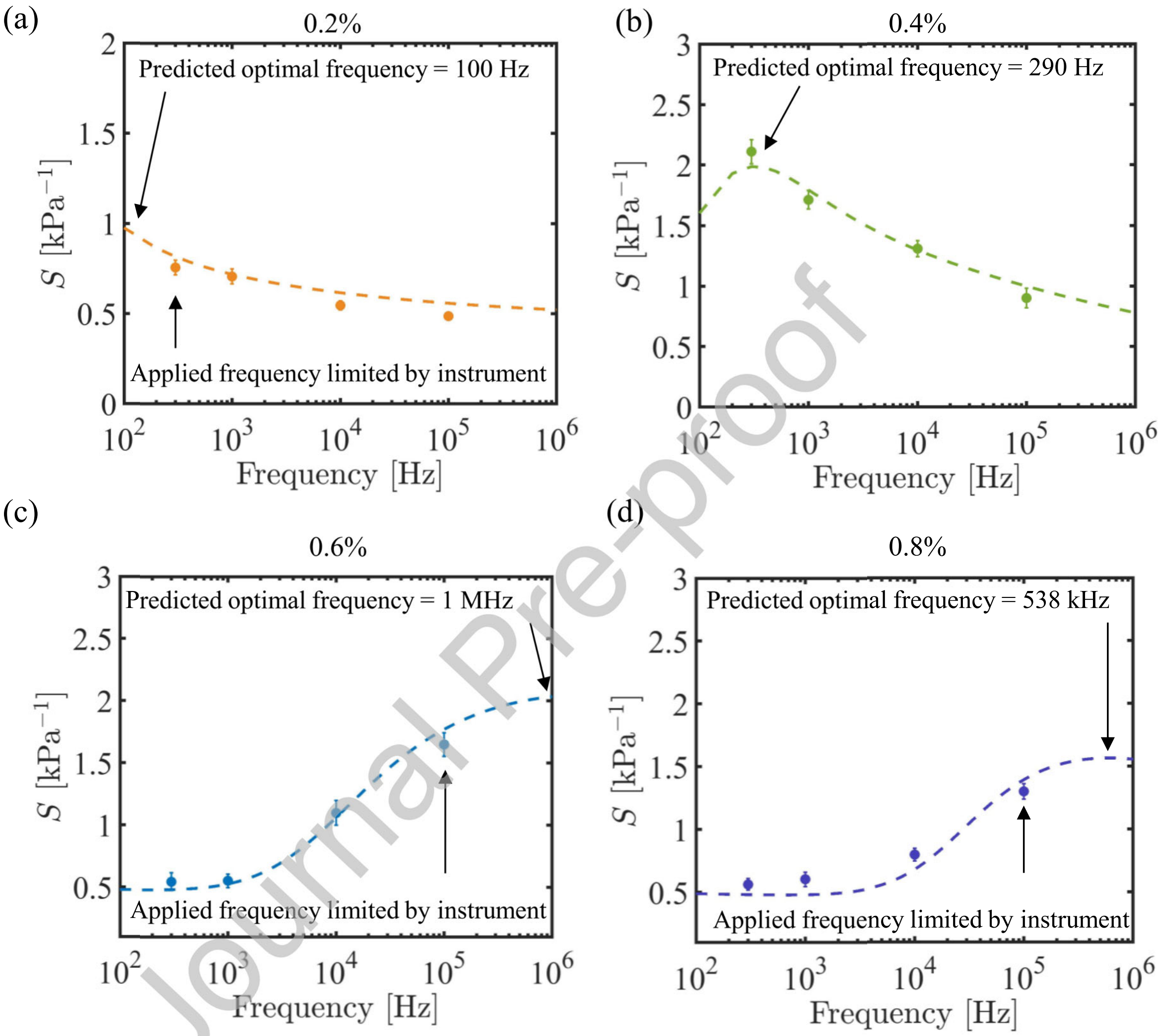

Figure 10: Model-predicted and experimentally validated sensitivity as a function of excitation frequency for CPS for doping ratios of (a) 0.2%, (b) 0.4%, (c) 0.6%, and (d) 0.8%. Distinct frequency-dependent sensitivity profiles are observed for different material compositions. Dashed lines represent predictions from the double-branch model using frequency-dependent C_p, $\tan\delta$, and $C_\mathrm{i}/C_\mathrm{p}$, while solid markers denote experimentally measured sensitivities.

3.4. Effects of the capacitance ratio $C_\mathrm{i}/C_\mathrm{p}$

In this section, we systematically examine how the capacitance ratio influences the sensitivity of all three types of CPS using a combined experimental and theoretical approach. Experimentally, the capacitance ratio is tuned by varying the thickness of the insulating dielectric layer while keeping the same PNC so that the

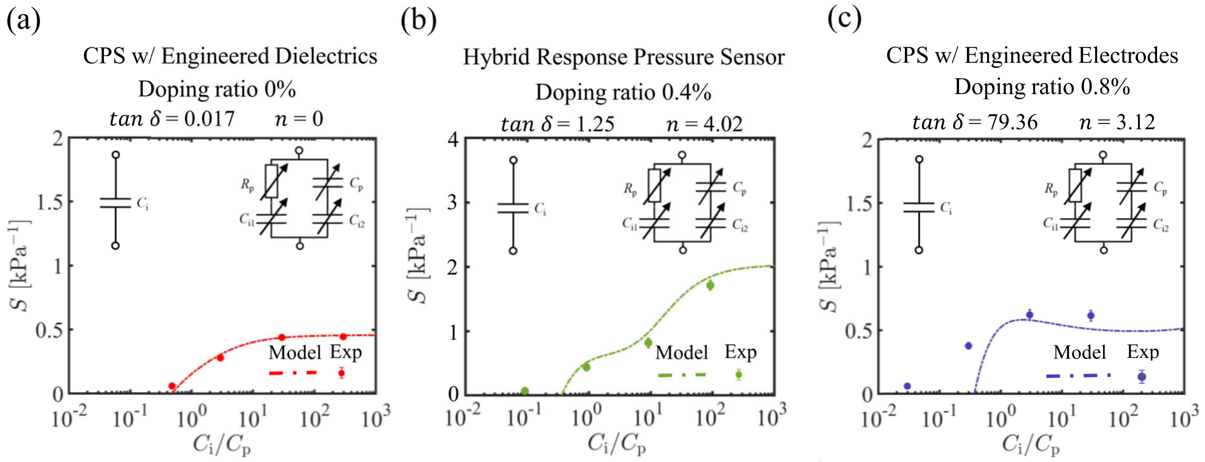

Figure 11: Experimental and model-predicted CPS sensitivities as a function of the capacitance competition ratio $C_\mathrm{i}/C_\mathrm{p}$, tuned by varying the insulating-layer thickness, for three representative CPS types. (a) CPS with engineered dielectrics (0% doping, $\tan\delta = 0.017$, $n = 0$) exhibits a monotonic increase in sensitivity with $C_\mathrm{i}/C_\mathrm{p}$, followed by saturation at large capacitance ratios. (b) Hybrid response pressure sensor (0.4% doping) with moderate dielectric loss ($\tan\delta = 1.25$) and strong piezoresistivity ($n = 4.02$) shows a pronounced two-regime transition in sensitivity. (c) CPS with engineered electrodes (0.8% doping), characterized by high dielectric loss ($\tan\delta = 79.36$) and intermediate piezoresistivity ($n = 3.12$), produces a distinct sensitivity peak followed by saturation.

other parameters remain unchanged. Three representative doping ratios are selected: 0%, 0.4%, and 0.8%, which represents CPS with engineered dielectrics, HRPS, and CPS with engineered electrodes, respectively. For each doping ratio, the thickness of the dielectric layer is varied between 2 µm, 20 µm, 200 µm, and 2000 µm. The experimental results are compared to theoretical predictions for CPS with engineered dielectrics (Fig. 11a), HRPS (Fig. 11b), and CPS with engineered electrodes (Fig. 11c). Satisfying agreements with the theory were obtained for all cases tested. It is worth noting that at small capacitance ratio, the double-branch model degrade. In the low capacitance ratio regime, the PNC or sensing layer is negligible, and the system effectively reduces to a purely capacitive structure dominated by the flat dielectric layer. Under this condition, the sensing response is governed primarily by the mechanical deformation of the dielectric layer. In our model, the dielectric layer is assumed to be relatively stiff (i.e., E→ ∞), leading to negligible deformation and, consequently, near-zero sensitivity.

In all three cases, a clear trend emerges: as the dielectric layer becomes thinner, i.e., as C_i and $C_\mathrm{i}/C_\mathrm{p}$ increase, the sensitivity of the CPS improves. However, this enhancement is not indefinite. As shown in all three subplots, the sensitivity begins to saturate once the dielectric layer is sufficiently thin. This trend is consistent with the experimental observations summarized in Table 1, where the sensitivity of CPS with engineered electrodes improves with increasing thickness ratio (corresponding to an increase in the capacitance ratio) (Totaro et al., 2020), and higher thickness ratios are generally associated with higher sensitivity for hybrid response pressure sensor and CPS with engineered dielectric (Totaro et al., 2020; Zhong et al., 2023; Xiong et al., 2020; Berman et al., 2024; Jin et al., 2024). The results also explain the findings in (Ruth et al., 2020), where all the dielectric layers considered are sufficiently thin and the sensitivity enhancement from $C_\mathrm{i}/C_\mathrm{p}$ reached a plateau, therefore sensitivity is almost independent of the thickness of the flat dielectric layer. It is worth noting that observations reported in capacitive pressure sensors (CPS) with engineered micro-dome dielectrics are consistent with the proposed theoretical framework. For example, in (Thouti et al., 2022), two configurations were compared: a micro-dome dielectric layer alone and a micro-dome dielectric layer combined with an additional flat PDMS layer. The former configuration exhibits higher sensitivity. Within our framework, this corresponds to the absence of the interfacial dielectric layer, i.e., $C_\mathrm{i} \to \infty$, resulting in a large ratio $C_\mathrm{i}/C_\mathrm{p}$. In contrast, the introduction of a flat dielectric layer reduces $C_\mathrm{i}/C_\mathrm{p}$, leading to a lower sensitivity. This trend is in direct agreement with the predictions of the present model. A similar interpretation can be extended to CPS with engineered architected dielectrics. For instance, in (Berman et al., 2024), increasing the sensing layer thickness (EPU lattice) from 2.4 mm to 3.6 mm effectively decreases C_p, thereby increasing the ratio $C_\mathrm{i}/C_\mathrm{p}$ and resulting in enhanced sensitivity. Moreover, consistent behavior has also been observed in CPS with engineered micro-dome electrodes. In (Xiong et al., 2020), for a fixed dome geometry, reducing the thickness of the flat dielectric layer from 10 μm to 4 μm leads to an increase in sensitivity. Within the present framework, this corresponds to an increase in $C_\mathrm{i}/C_\mathrm{p}$, further supporting the generality of the proposed model.

3.5. Effects of Archie's Law exponent n and contact ratio α

In this section, we theoretically analyze the influence of two key parameters—Archie's law coefficient n and the contact ratio α—on the sensitivity of CPS. This analysis complements the previous experimental sections by providing design-oriented insights that are difficult to obtain experimentally. In practice, independently tuning n requires precise manipulation of conduction pathways within the porous composite, and adjusting α demands controlled modification of the geometry of interfacial contact, both of which are challenging to achieve systematically in experiments. Consequently, the results presented here are fully model-based and should be interpreted as qualitative design guidelines.

Figure 12a illustrates how the sensitivity S varies with the exponent in Archie's law n under three representative loss-angle conditions ($\tan\delta = 10, 1, 0.1$) at a fixed capacitance ratio $C_i/C_p = 10^3$. For cases $\tan\delta = 10$ (corresponding to CPS with engineered electrodes) and $\tan\delta = 1$ (corresponding to HRPS), the curves display an approximately linear relation between S and n on a log–log scale. This behavior indicates that increasing n continuously enhances sensitivity without diminishing returns. Thus, for CPS with engineered electrodes and HRPS, pursuing higher n is always beneficial for maximizing sensitivity. For the low-loss case $\tan\delta = 0.1$ (representing CPS with engineered dielectrics), the trend differs: S remains nearly constant at small n and only increases noticeably when n becomes sufficiently large. This reflects the fact that when dielectric loss is small, the resistive branch contributes very little, and increasing n becomes effective only when the material approaches a percolation-like transition. Figure 12b further examines the dependence on n by varying C_i/C_p over two orders of magnitude while fixing $\tan\delta = 1$ (HRPS). All curves collapse onto a similar monotonic trend, demonstrating that the qualitative influence of n is largely insensitive to changes in sensor geometry. These results establish n as a powerful intrinsic parameter for potentially enhancing CPS performance.

Figure 12c–d presents the theoretical influence of the contact ratio α, defined as the fraction of sensing layer in direct electrical contact with the dielectric layer, on the sensitivity S of CPS. Figure 12c shows sensitivity as a function of α under three representative levels of dielectric-loss ($\tan\delta = 10$, 1, 0.1). Within a broad intermediate range $0.1 \lesssim \alpha \lesssim 0.9$, the sensitivity depends only weakly on α, indicating that moderate changes in interfacial contact have a limited impact on overall device performance. This insensitive regime of α appears consistently for engineered electrodes ($\tan\delta = 10$), HRPS ($\tan\delta = 1$) and engineered dielectrics ($\tan\delta = 0.1$), suggesting that most CPS may operate in a regime where α is not a dominant design factor. However, as α approaches extreme values ($\alpha \to 0$ or $\alpha \to 1$), the sensitivity exhibits abrupt changes, with a sharp decrease or divergence depending on the level of dielectric loss. Figure 12d further plots the sensitivity vs. α at fixed dielectric loss $\tan\delta = 1$ (representative of HRPS) for various $C_\mathrm{i}/C_\mathrm{p}$. Similar to the case with various loss angles δ, the sensitivity depends weakly on the capacitance ratio $C_\mathrm{i}/C_\mathrm{p}$ for intermediate α but increases rapidly with α when α approaches zero or one. A lower capacitance ratio is found to shrink the middle flat region. These results indicate that increasing the contact ratio does not universally enhance the sensitivity; rather, only very small or very large contact areas exert a pronounced influence.

4. Conclusion

In this work, we present a unified analytical model capable of predicting the sensitivity of PNC-based CPS. Unlike conventional single-branch models for CPS with engineered dielectrics and engineered electrodes, the double-branch model captures the effects of the PNC loss angle δ varying from 0° to 90° on the sensitivity of CPS. The model also includes Young modulus E, capacitance ratio $C_\mathrm{i}/C_\mathrm{p}$, the Archie's law exponent n, and contact ratio α. Through a combination of material characterization, analytical derivation, and device validation, we demonstrate that the model accurately predicts the effects of key material and structural parameters, including CNT doping ratio, excitation frequency, dielectric layer thickness, and interfacial contacts, on the CPS sensitivity. Specifically:

- We show that the loss angle of the sensing materials δ ($\tan\delta$), a critical governing parameter of the sensitivity of CPS, can be tuned through both doping and excitation frequencies. This enables the identification of the optimal phase for maximizing sensitivity.

- We derive and validate empirical expressions that link the doping ratio to $\tan\delta$, n, and $C_\mathrm{i}/C_\mathrm{p}$, allowing continuous prediction of sensitivity across the design space.

- We evaluate the role of the capacitance ratio by varying the dielectric thickness and show that sensitivity enhancement via dielectric thinning exhibits saturation behavior.

- Finally, theoretical studies on n and α highlight key microstructural design strategies, such as promoting a piezoresistive response and changing interfacial contact, to further boost sensitivity.

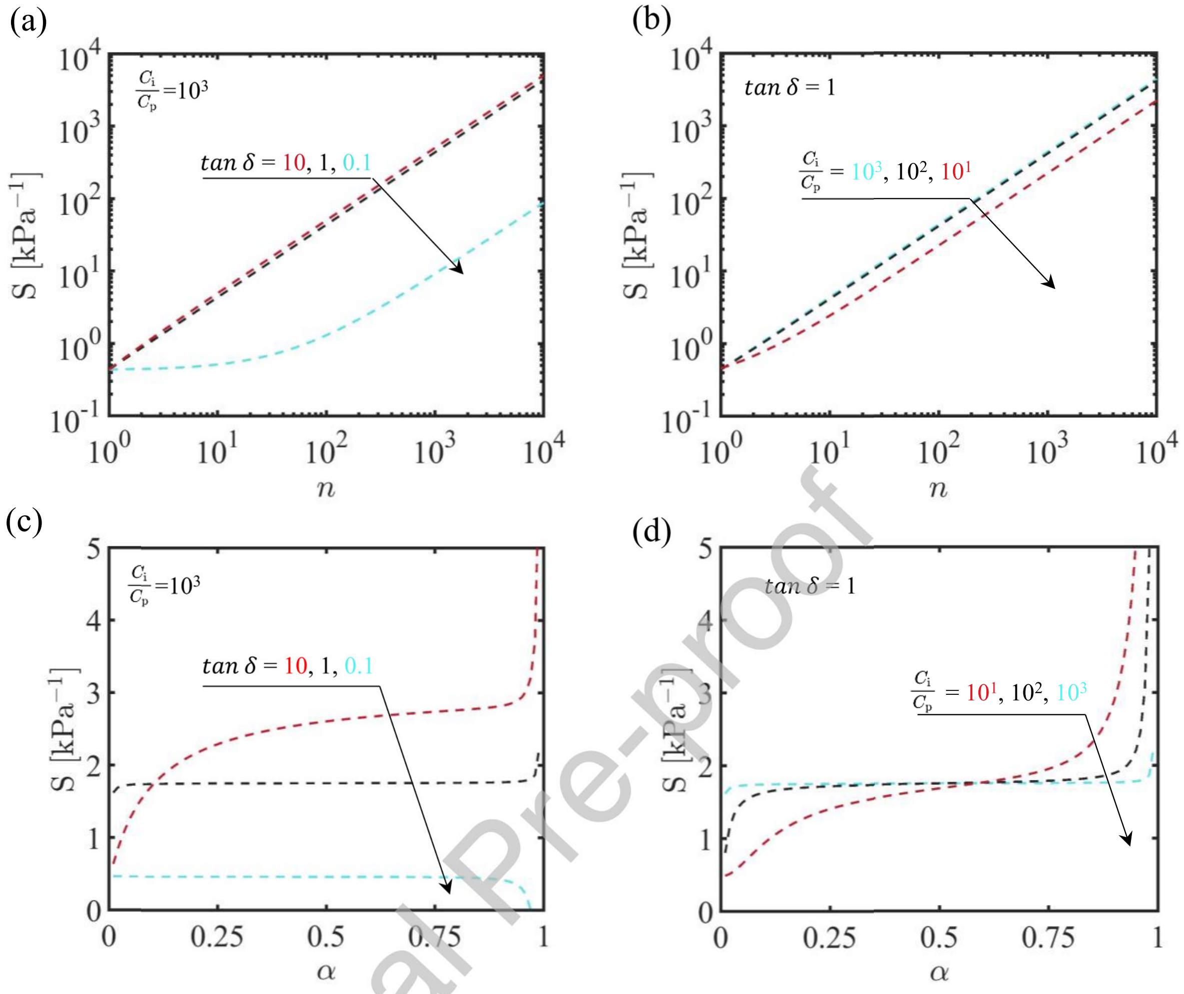

Figure 12: Theoretical prediction of the effects of the Archie's law exponent n and the contact ratio α on the CPS sensitivity S. (a,b) Sensitivity S increases monotonically with n across all CPS types, (a) for varying loss tangents $\tan\delta = 0.1, 1$, and 10 at fixed $C_\mathrm{i}/C_\mathrm{p} = 10^3$, and (b) for varying capacitance competition ratios $C_\mathrm{i}/C_\mathrm{p} = 10, 10^2$, and 10^3 at fixed $\tan\delta = 1$. (c,d) Sensitivity S as a function of the contact ratio α. Over a broad practical range $(0.1 \leq \alpha \leq 0.9)$, S exhibits only weak dependence on α for (c) different loss tangents at fixed $C_\mathrm{i}/C_\mathrm{p} = 10^3$ and for (d) different capacitance competition ratios at fixed $\tan\delta = 1$.

In general, this study provides a comprehensive theoretical and experimental basis for the rational design of CPS through materials engineering and structural optimization. The model not only unifies and explains the diverse behaviors of engineered dielectrics, hybrid effects, and engineered electrodes, but also offers predictive power to guide sensor performance with minimal trial-and-error. The double-branch model thus serves as a foundational tool for accelerating the development of high-performance, tunable, and application-specific CPS. Importantly, the framework is not limited to stochastic porous structures, but is inherently structure-agnostic. It is built upon four modular components: (i) constitutive behavior, (ii) structural evolution (e.g., porosity or contact variation), (iii) piezocapacitive and piezoresistive relations, and (iv) equivalent circuit representation. As such, it can be readily extended to a wide range of architected sensing layers, including microdome, kirigami-inspired, anisotropic porous, and iontronic systems. While the underlying deformation mechanisms differ (e.g., contact evolution, structural reconfiguration, or interfacial effects), the same electromechanical coupling framework remains applicable. These results highlight the generality of the proposed framework and establish it as a foundational tool for understanding and designing high-performance, tunable, and application-specific CPS across diverse material systems and structural architectures.

While the present study focuses on the initial sensitivity under quasi-static loading conditions, future work may further investigate the role of viscoelasticity in governing device performance, including electrical and mechanical hysteresis, the relationship between material fatigue thresholds and long-term sensor cyclability, and more.

Declaration of Competing Interest

The authors declare that they have no known competing financial interests or personal relationships that could have appeared to influence the work reported in this paper.

Acknowledgment

This work is supported by the US NSF CMMI MOMS Grant 2418433.

Declaration of generative AI and AI-assisted technologies in the writing process

During the preparation of this manuscript, the authors used ChatGPT to polish the language and Gemini 3.0 to simplify the derivation of Appendix B.3. After using this tool/service, the authors reviewed and edited the content as needed and assume full responsibility for the content of the publication.

Appendix A. Bulk versus Interfacial Electromechanical Mechanisms

Figure A.1 provides a conceptual illustration of the bulk and interface-dominated electric-field distributions in different capacitive pressure sensor architectures. Figure A.1(a) compares CPS with engineered dielectrics, HRPS, and CPS with engineered electrodes under applied compression. For CPS with engineered dielectrics (Fig. A.1(a) (i)), the sensing response is governed by a bulk electric field extending vertically from the top electrode to the bottom electrode across the dielectric layer (marked by orange). In contrast, CPS with engineered electrodes are dominated by electric fields of interfacial contact localized in the contact regions between the conductive porous electrode and the dielectric layer (marked by green) (Fig. A.1(a) (iii)). HRPS exhibit an intermediate regime in which bulk effects and effects of interfacial contact coexist, leading to simultaneous contributions of bulk and interface to the response to detection (Fig. A.1(a) (ii)).

Figure A.1(b) further explains why the sensing response of CPS with engineered electrodes is dominated by effects of interfacial contact. As shown in Fig. A.1(b), most regions of the porous conductive electrode

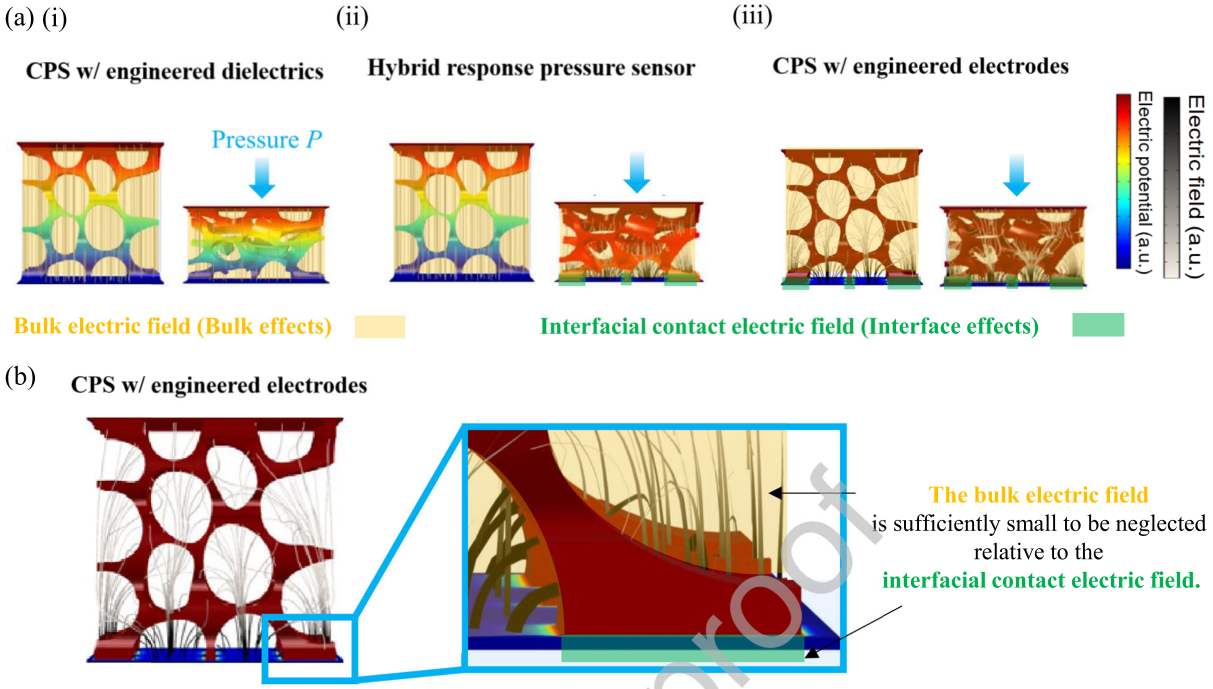

Figure A.1: Conceptual illustration of bulk- and interface-dominated electric-field distributions in capacitive pressure sensors. (a) Comparison of CPS with engineered dielectrics, HRPS, and CPS with engineered electrodes under applied compression. (b) Electric-potential and electric-field distributions in CPS with engineered electrodes. Most regions of the conductive porous electrode remain at nearly uniform electric potential, resulting in negligible bulk electric-field contribution, while the electric field is strongly localized at the contact regions with the dielectric layer. As a result, the sensing response is dominated by interfacial contact capacitance rather than bulk electric-field modulation. Reproduced and modified with permission from (Ha et al., 2024) Copyright Cell Press

remain at nearly the same electric potential (red), resulting in negligible potential differences and correspondingly weak bulk electric fields within the electrode. Physically, capacitance arises from the ability to store charge under a finite potential difference. When two regions remain at nearly the same electric potential, the potential difference approaches zero, leading to negligible electric field and charge storage. Consequently, regions of the porous electrode with nearly uniform potential contribute little to the overall capacitance, and the bulk electric-field contribution can be neglected. In contrast, a magnified view of the electrode–dielectric interface reveals that the electric field is strongly localized at the contact regions between the porous electrode and the dielectric layer. The interfacial contact capacitance therefore dominates the overall capacitive response. As a result, the sensing behavior of CPS with engineered electrodes is primarily governed by contact-mediated electromechanical coupling rather than bulk electric-field modulation.

Appendix B. Derivation of the Double Branch Model

The derivation of the double-branch model is based on the pressure–phase-angle relationship. We first derive the expressions in terms of the phase angle and then convert them into the corresponding loss angle.

Appendix B.1. Derivation of pressure phase angle relation

Before deriving the double branch model, we list the following assumptions:

- **Mechanical assumptions:** The applied pressure is assumed to be small so that:
  - The sensing material behaves as a linear elastic solid, with Young's modulus E treated as constant.
  - The contact ratio α is directly related to porosity, $\alpha = 1 - \phi$, and remains nearly constant within the pressure range considered.
  - The dielectric layer is incompressible.
- **Electrical assumptions:** The piezoresistive and piezocapacitive models are valid under small applied pressures, where:
  - The complex electromechanical behavior of the sensing layer is simplified into an equivalent circuit consisting of a parallel capacitor C_p and resistor R_p. Here, C_p and R_p are defined as parallel capacitance and resistance, respectively, both directly measurable with an LCR meter.
  - A modified Archie's law is assumed to describe the behavior of the resistive branch under pressure.
  - The classical parallel-plate capacitor expression is assumed to describe the capacitive branch behavior under pressure.
- **Model assumption:** mechanical and electrical responses are assumed to be decoupled.

In this section, we first derive the piezoresistive, piezocapacitive, and pressure phase angle relation. We start with the piezoresistive relation following previous work (Wang et al., 2024)

$$R_\mathrm{p} = R_0(1-\varepsilon)^n \tag{B.1}$$

Where R_p is the parallel resistance of porous nanocomposites, R_0 is the initial resistance, ε is the compressive strain, therefore, we have:

$$\frac{\partial R_\mathrm{p}}{\partial P} = \frac{\partial R_\mathrm{p}}{\partial \varepsilon}\frac{\partial \varepsilon}{\partial P} = -nR_0(1-\varepsilon)^{n-1}\frac{\partial \varepsilon}{\partial P} \tag{B.2}$$

$$\left.\frac{\partial R_\mathrm{p}}{\partial P}\right|_{P=0} = -nR_0(1-\varepsilon)^{n-1}\big|_{\varepsilon=0}\left.\frac{\partial \varepsilon}{\partial P}\right|_{P=0} = -nR_{\mathrm{p}0}\frac{1}{E} \tag{B.3}$$

Where $R_{\mathrm{p}0}$ is the initial parallel resistance of the porous nanocomposites. Similarly, the piezo capacitive behavior can be expressed:

$$C_\mathrm{p} = \frac{k\epsilon_0 A}{d} \tag{B.4}$$

Where C_p is the parallel capacitance of porous nanocomposites, k is the dielectric constant, ϵ_0 is the vacuum permittivity, A is the area of two electrodes, and d is the distance between two electrodes:

$$\frac{\partial C_\mathrm{p}}{\partial P} = \frac{\partial C_\mathrm{p}}{\partial d}\frac{\partial d}{\partial \varepsilon}\frac{\partial \varepsilon}{\partial P} = -\frac{k\epsilon_0 A}{d^2}(-d_0)\frac{1}{E} \tag{B.5}$$

$$\frac{\partial C_{\mathrm{p}}}{\partial P}\bigg|_{P=0} = \frac{k\epsilon_0 A}{d_0^2}(d_0)\frac{1}{E} = \frac{C_{\mathrm{p0}}}{E} \tag{B.6}$$

Where C_{p0} is the initial parallel capacitance of the porous nanocomposites. therefore, the corresponding pressure phase angle relation:

$$\frac{\partial|tan\theta|}{\partial P}\bigg|_{P=0} = \omega\frac{\partial R_{\mathrm{p}}}{\partial P}C_{\mathrm{p}}\bigg|_{P=0} + \omega\frac{\partial C_{\mathrm{p}}}{\partial P}R_{\mathrm{p}}\bigg|_{P=0} = -n\omega\frac{R_{\mathrm{p0}}}{E}C_{\mathrm{p0}} + \omega\frac{C_{\mathrm{p0}}}{E}R_{\mathrm{p0}} = \frac{(1-n)}{E}|tan\theta_0| \tag{B.7}$$

Where θ_0 is the initial phase angle of the porous nanocomposites. For the change in the contact ratio, we have this estimation:

$$\alpha = 1-\phi, \tag{B.8}$$

where α is the contact ratio and ϕ is porosity. According to the porosity strain relation (Zhang et al., 2021; Li et al., 2024):

$$\phi = 1 - \frac{1-\phi_0}{1-\varepsilon}, \tag{B.9}$$

Where ϕ_0 is the initial porosity of porous nanocomposites.

$$\frac{\partial\alpha}{\partial P} = \frac{\partial\alpha}{\partial\phi}\frac{\partial\phi}{\partial\varepsilon}\frac{\partial\varepsilon}{\partial P} = (-1)\frac{-(1-\phi_0)}{(1-\varepsilon)^2}\frac{1}{E} \tag{B.10}$$

$$\frac{\partial\alpha}{\partial P}\bigg|_{P=0} = \frac{\alpha_0}{E} \tag{B.11}$$

Where α_0 is the initial contact ratio.

Appendix B.2. Derivation of capacitance of double branch model

As shown in Figure 3c, the resistive branch is denoted branch 1, the capacitive branch is denoted branch 2,

$$Z_{\mathrm{branch1}} = Z_{\mathrm{R}} + Z_{\mathrm{i1}} = R_{\mathrm{p}} + \frac{1}{j\omega\alpha C_{\mathrm{i}}} \tag{B.12}$$

$$Z_{\mathrm{branch2}} = Z_{\mathrm{C}} + Z_{\mathrm{i2}} = \frac{1}{j\omega C_{\mathrm{p}}} + \frac{1}{j\omega(1-\alpha)C_{\mathrm{i}}} \tag{B.13}$$

$$Z = \frac{Z_{\mathrm{branch1}}Z_{\mathrm{branch2}}}{Z_{\mathrm{branch1}}+Z_{\mathrm{branch2}}} = \frac{(\frac{1}{C_{\mathrm{p}}}+\frac{1}{(1-\alpha)C_{\mathrm{i}}})(R_{\mathrm{p}}+\frac{1}{j\omega\alpha C_{\mathrm{i}}})}{\frac{1}{C_{\mathrm{p}}}+\frac{1}{(1-\alpha)C_{\mathrm{i}}}+\frac{1}{\alpha C_{\mathrm{i}}}+\omega R_{\mathrm{p}}j} \tag{B.14}$$

$$Z = \frac{(\frac{1}{C_{\mathrm{p}}}+\frac{1}{(1-\alpha)C_{\mathrm{i}}})(R_{\mathrm{p}}+\frac{1}{j\omega\alpha C_{\mathrm{i}}})(\frac{1}{C_{\mathrm{p}}}+\frac{1}{(1-\alpha)C_{\mathrm{i}}}+\frac{1}{\alpha C_{\mathrm{i}}}-\omega R_{\mathrm{p}}j)}{(\frac{1}{C_{\mathrm{p}}}+\frac{1}{(1-\alpha)C_{\mathrm{i}}}+\frac{1}{\alpha C_{\mathrm{i}}})^2+\omega^2R_{\mathrm{p}}^2} \tag{B.15}$$

The reactance, which is the imaginary part, can be expressed as

$$X = \frac{-(\frac{1}{\omega})(\frac{1}{C_{\mathrm{p}}}+\frac{1}{(1-\alpha)C_{\mathrm{i}}}+\frac{1}{\alpha C_{\mathrm{i}}})(\frac{1}{\alpha C_{\mathrm{i}}C_{\mathrm{p}}}+\frac{1}{\alpha(1-\alpha)C_{\mathrm{i}}^2})+\omega\frac{R_{\mathrm{p}}^2}{C_{\mathrm{p}}}+\frac{\omega R_{\mathrm{p}}^2}{(1-\alpha)C_{\mathrm{i}}}}{(\frac{1}{C_{\mathrm{p}}}+\frac{1}{(1-\alpha)C_{\mathrm{i}}}+\frac{1}{\alpha C_{\mathrm{i}}})^2+\omega^2R_{\mathrm{p}}^2} \tag{B.16}$$

The corresponding capacitance C_{CPS} can be expressed as follows:

$$\begin{aligned} C_{\mathrm{CPS}} = -\frac{1}{\omega X} &= \frac{(\frac{1}{C_{\mathrm{p}}}+\frac{1}{(1-\alpha)C_{\mathrm{i}}}+\frac{1}{\alpha C_{\mathrm{i}}})^2+\omega^2R_{\mathrm{p}}^2}{(\frac{1}{C_{\mathrm{p}}}+\frac{1}{(1-\alpha)C_{\mathrm{i}}}+\frac{1}{\alpha C_{\mathrm{i}}})(\frac{1}{\alpha C_{\mathrm{i}}C_{\mathrm{p}}}+\frac{1}{\alpha(1-\alpha)C_{\mathrm{i}}^2})+\omega^2\frac{R_{\mathrm{p}}^2}{C_{\mathrm{p}}}+\frac{\omega^2R_{\mathrm{p}}^2}{(1-\alpha)C_{\mathrm{i}}}} \\ &= \frac{C_{\mathrm{i}}\left[(1+\frac{C_{\mathrm{p}}}{(1-\alpha)C_{\mathrm{i}}}+\frac{C_{\mathrm{p}}}{\alpha C_{\mathrm{i}}})^2+tan^2\theta\right]}{(1+\frac{C_{\mathrm{p}}}{(1-\alpha)C_{\mathrm{i}}}+\frac{C_{\mathrm{p}}}{\alpha C_{\mathrm{i}}})(\frac{1}{\alpha}+\frac{C_{\mathrm{p}}}{\alpha(1-\alpha)C_{\mathrm{i}}})+tan^2\theta\frac{C_{\mathrm{i}}}{C_{\mathrm{p}}}+\frac{tan^2\theta}{(1-\alpha)}} \end{aligned} \tag{B.17}$$

Replace phase angle θ with loss angle δ:

$$C_{\mathrm{CPS}} = \frac{C_{\mathrm{i}}\big[(1+\frac{C_{\mathrm{p}}}{(1-\alpha)C_{\mathrm{i}}}+\frac{C_{\mathrm{p}}}{\alpha C_{\mathrm{i}}})^2\cdot tan^2\delta+1\big]}{(1+\frac{C_{\mathrm{p}}}{(1-\alpha)C_{\mathrm{i}}}+\frac{C_{\mathrm{p}}}{\alpha C_{\mathrm{i}}})(\frac{1}{\alpha}+\frac{C_{\mathrm{p}}}{\alpha(1-\alpha)C_{\mathrm{i}}})\cdot tan^2\delta+\frac{C_{\mathrm{i}}}{C_{\mathrm{p}}}+\frac{1}{(1-\alpha)}} \tag{B.18}$$

Appendix B.3. Derivation of capacitance of double branch model using complex permittivity

As shown in Figure 3c, the resistive branch and the capacitive branch of the porous functional layer can also be modeled by a leaky capacitor with *complex permittivity*, $k^* = k - i\,k' = k(1 - i\tan\delta)$, , where k is the storage permittivity, k' is the loss permittivity and $\tan\delta = k'/k$ is the dielectric loss tangent. For an electrode area A and an instantaneous layer thickness d, the *complex capacitance* of the functional layer is

$$C_{\mathrm{p}}^* \;=\; \frac{k^*\varepsilon_0\,A}{d} \;=\; C_{\mathrm{p}}\,(1 - i\tan\delta), \qquad C_{\mathrm{p}} = \frac{k\varepsilon_0\,A}{d}. \tag{B.19}$$

A flat, lossless dielectric layer has capacitance C_i

Equivalence to the parallel $R_p \parallel C_p$ picture. Writing the branch admission as $Y = i\omega C_{\mathrm{p}}^* = \omega C_{\mathrm{p}}\tan\delta + i\,\omega C_{\mathrm{p}}$, one identifies the parallel representation $Y = 1/R_{\mathrm{p}} + i\omega C_{\mathrm{p}}$ with

$$R_{\mathrm{p}} = \frac{1}{\omega C_{\mathrm{p}}\tan\delta}, \qquad \Rightarrow \quad \omega R_{\mathrm{p}} C_{\mathrm{p}} = \frac{1}{\tan\delta}. \tag{B.20}$$

Hence, the commonly used descriptor $|\tan\theta| = \omega R_p C_p$ maps exactly to $|\tan\theta| = 1/\tan\delta$ in the complex-permittivity formalism. Using the relation from Eq. (B.20), we substitute the resistance R_p with its complex permittivity equivalent:

$$R_p = \frac{\cot\delta}{\omega C_p} \tag{B.21}$$

Let $q = 1/C$ denote elastance (inverse capacitance) to simplify the algebra.

$$q_p = \frac{1}{C_p}, \quad q_1 = \frac{1}{\alpha C_i}, \quad q_2 = \frac{1}{(1-\alpha)C_i} \tag{B.22}$$

The impedances of Branch 1 (Z_1) and Branch 2 (Z_2) are:

$$\begin{aligned} Z_{branch1} &= R_{\mathrm{p}} + \frac{1}{i\omega\alpha C_{\mathrm{i}}} = \frac{\cot\delta}{\omega C_{\mathrm{p}}} + \frac{q_1}{i\omega} = \frac{1}{i\omega}\,(iq_{\mathrm{p}}\cot\delta + q_1) \\ Z_{branch2} &= \frac{1}{i\omega C_{\mathrm{p}}} + \frac{1}{i\omega(1-\alpha)C_{\mathrm{i}}} = \frac{1}{i\omega}(q_{\mathrm{p}} + q_2) \end{aligned} \tag{B.23}$$

The total impedance

$$Z = \frac{Z_{branch1}Z_{branch2}}{Z_{branch1}+Z_{branch2}} = \frac{1}{i\omega}\frac{(q_1 + iq_{\mathrm{p}}\cot\delta)(q_{\mathrm{p}}+q_2)}{(q_1 + iq_{\mathrm{p}}\cot\delta) + (q_{\mathrm{p}}+q_2)} \tag{B.24}$$

Let q_Σ be the sum of all inverse capacitances in the loop:

$$q_\Sigma = q_1 + q_2 + q_{\mathrm{p}} = \frac{1}{\alpha C_{\mathrm{i}}} + \frac{1}{(1-\alpha)C_{\mathrm{i}}} + \frac{1}{C_{\mathrm{p}}}$$

The denominator becomes $D = q_\Sigma + iq_{\mathrm{p}}\cot\delta$. The numerator is $N = (q_1 + iq_{\mathrm{p}}\cot\delta)(q_{\mathrm{p}} + q_2)$.

$$Z = \frac{1}{i\omega}\frac{N}{D} \tag{B.25}$$

The effective serial capacitance C_{CPS} is defined by the imaginary part of the impedance:

$$C_{\mathrm{CPS}} = -\frac{1}{\omega \cdot \mathrm{Im}(Z)} \tag{B.26}$$

Expanding the terms results in the following.

$$C_{\mathrm{CPS}} = \frac{q_\Sigma^2 + q_{\mathrm{p}}^2 \cot^2 \delta}{(q_{\mathrm{p}} + q_2)\left[q_1 q_\Sigma + q_{\mathrm{p}}^2 \cot^2 \delta\right]} \tag{B.27}$$

Rearrange it a little:

$$C_{\mathrm{CPS}} = \frac{1}{q_{\mathrm{p}} + q_2}\left[\frac{1 + \left(\frac{q_\Sigma}{q_{\mathrm{p}}}\right)^2 \tan^2 \delta}{1 + \left(\frac{q_1 q_\Sigma}{q_{\mathrm{p}}^2}\right)\tan^2 \delta}\right] \tag{B.28}$$

Substituting the physical parameters back into the ratios:

$$\begin{aligned}
\frac{q_\Sigma}{q_{\mathrm{p}}} &= 1 + \frac{C_{\mathrm{p}}}{\alpha(1-\alpha)C_{\mathrm{i}}} \\
\frac{q_1 q_\Sigma}{q_{\mathrm{p}}^2} &= \frac{C_{\mathrm{p}}}{\alpha C_{\mathrm{i}}}\left(1 + \frac{C_{\mathrm{p}}}{\alpha(1-\alpha)C_{\mathrm{i}}}\right) \\
\frac{1}{q_{\mathrm{p}} + q_1} &= \frac{C_{\mathrm{i}}}{\frac{C_{\mathrm{i}}}{C_{\mathrm{p}}} + \frac{1}{1-\alpha}}
\end{aligned} \tag{B.29}$$

The final expression for the serial capacitance is:

$$C_{\mathrm{CPS}} = \frac{C_{\mathrm{i}}}{\frac{C_{\mathrm{i}}}{C_{\mathrm{p}}} + \frac{1}{1-\alpha}}\left[\frac{1 + \left(1 + \frac{C_p}{\alpha(1-\alpha)C_i}\right)^2 \tan^2 \delta}{1 + \frac{C_p}{\alpha C_i}\left(1 + \frac{C_p}{\alpha(1-\alpha)C_i}\right)\tan^2 \delta}\right] \tag{B.30}$$

which is the same as B.18.

Appendix B.4. Derivation of sensitivity expression of double branch model

We derive the expressions in terms of the phase angle and then convert them into the corresponding loss angle, since taking derivatives with respect to the phase angle is mathematically more straightforward.

$$\frac{\triangle C}{C_0} = \frac{C_{\mathrm{CPS}} - C_{\mathrm{CPS0}}}{C_{\mathrm{CPS0}}} \tag{B.31}$$

Using the expression B.17, we have:

$$S = \frac{\partial(\frac{\triangle C}{C_0})}{\partial P}\frac{1}{C_{\mathrm{CPS0}}}\frac{\partial C_{\mathrm{CPS}}}{\partial P} = \frac{1}{C_{\mathrm{CPS0}}}\left[\frac{\partial(C_{\mathrm{CPS}})}{\partial C_{\mathrm{p}}}\frac{\partial C_{\mathrm{p}}}{\partial \epsilon}\frac{\partial \epsilon}{\partial P} + \frac{\partial(C_{\mathrm{CPS}})}{\partial \tan\delta}\frac{\partial \tan\delta}{\partial \epsilon}\frac{\partial \epsilon}{\partial P} + \frac{\partial(C_{\mathrm{CPS}})}{\partial \alpha}\frac{\partial \alpha}{\partial \phi}\frac{\partial \phi}{\partial \epsilon}\frac{\partial \epsilon}{\partial P}\right] \tag{B.32}$$

$$\begin{aligned}
S = \frac{\partial(\frac{\triangle C}{C_0})}{\partial P} &= \frac{(1 + \frac{C_{\mathrm{p0}}}{(1-\alpha_0)C_{\mathrm{i}}} + \frac{C_{\mathrm{p0}}}{\alpha_0 C_{\mathrm{i}}})(\frac{1}{\alpha_0} + \frac{C_{\mathrm{p0}}}{\alpha_0(1-\alpha_0)C_{\mathrm{i}}}) + tan^2\theta_0 \frac{C_{\mathrm{i}}}{C_{\mathrm{p0}}} + \frac{tan^2\theta_0}{(1-\alpha_0)}}{(1 + \frac{C_{\mathrm{p0}}}{(1-\alpha_0)C_{\mathrm{i}}} + \frac{C_{\mathrm{p0}}}{\alpha_0 C_{\mathrm{i}}})^2 + tan^2\theta_0} \cdot \\
&\frac{\partial\left[\frac{(1+\frac{C_{\mathrm{p}}}{(1-\alpha)C_{\mathrm{i}}}+\frac{C_{\mathrm{p}}}{\alpha C_{\mathrm{i}}})^2+tan^2\theta}{(1+\frac{C_{\mathrm{p}}}{(1-\alpha)C_{\mathrm{i}}}+\frac{C_{\mathrm{p}}}{\alpha C_{\mathrm{i}}})(\frac{1}{\alpha}+\frac{C_{\mathrm{p}}}{\alpha(1-\alpha)C_{\mathrm{i}}})+tan^2\theta\frac{C_{\mathrm{i}}}{C_{\mathrm{p}}}+\frac{tan^2\theta}{(1-\alpha)}}\right]}{\partial P}
\end{aligned} \tag{B.33}$$

$$
\begin{aligned}
S = {} & \frac{(1+\frac{C_{\mathrm{p}0}}{(1-\alpha_0)C_{\mathrm{i}}}+\frac{C_{\mathrm{p}0}}{\alpha_0 C_{\mathrm{i}}})(\frac{1}{\alpha_0}+\frac{C_{\mathrm{p}0}}{\alpha_0(1-\alpha_0)C_{\mathrm{i}}})+tan^2\theta_0\frac{C_{\mathrm{i}}}{C_{\mathrm{p}0}}+\frac{tan^2\theta_0}{(1-\alpha_0)}}{(1+\frac{C_{\mathrm{p}0}}{(1-\alpha_0)C_{\mathrm{i}}}+\frac{C_{\mathrm{p}0}}{\alpha_0 C_{\mathrm{i}}})^2+tan^2\theta_0}\cdot \\
& \frac{(tan^2\theta+(\frac{C_{\mathrm{p}}}{\alpha C_{\mathrm{i}}}+\frac{C_{\mathrm{p}}}{(1-\alpha)C_{\mathrm{i}}}+1)^2)}{(\frac{1}{\alpha}+\frac{C_{\mathrm{p}}}{C_{\mathrm{i}}(1-\alpha)\alpha})(1+\frac{C_{\mathrm{p}}}{\alpha C_{\mathrm{i}}}+\frac{C_{\mathrm{p}}}{(1-\alpha)C_{\mathrm{i}}})+\frac{tan^2\theta}{1-\alpha}+\frac{C_{\mathrm{i}}}{C_{\mathrm{p}}}tan^2\theta)^2}\cdot \\
& \Big[(\frac{C_{\mathrm{p}}}{\alpha C_{\mathrm{i}}}+\frac{C_{\mathrm{p}}}{(1-\alpha)C_{\mathrm{i}}}+1)(\frac{-1}{\alpha^2}\frac{\partial\alpha}{\partial P}+\frac{1}{C_{\mathrm{i}}\alpha(1-\alpha)}\frac{\partial C_{\mathrm{p}}}{\partial P}-\frac{C_{\mathrm{p}}}{C_{\mathrm{i}}\alpha^2(1-\alpha)}\frac{\partial\alpha}{\partial P}+\frac{C_{\mathrm{p}}}{C_{\mathrm{i}}\alpha(1-\alpha)^2}\frac{\partial\alpha}{\partial P})+ \\
& (\frac{1}{\alpha}+\frac{C_{\mathrm{p}}}{C_{\mathrm{i}}\alpha(1-\alpha)})(\frac{1}{C_{\mathrm{i}}(1-\alpha)}\frac{\partial C_{\mathrm{p}}}{\partial P}+\frac{1}{C_{\mathrm{i}}\alpha}\frac{\partial C_{\mathrm{p}}}{\partial P}-\frac{C_{\mathrm{p}}}{C_{\mathrm{i}}\alpha^2}\frac{\partial\alpha}{\partial P}+\frac{C_{\mathrm{p}}}{C_{\mathrm{i}}(1-\alpha)^2}\frac{\partial\alpha}{\partial P}\Big]- \\
& \frac{(1+\frac{C_{\mathrm{p}0}}{(1-\alpha_0)C_{\mathrm{i}}}+\frac{C_{\mathrm{p}0}}{\alpha_0 C_{\mathrm{i}}})(\frac{1}{\alpha_0}+\frac{C_{\mathrm{p}0}}{\alpha_0(1-\alpha_0)C_{\mathrm{i}}})+tan^2\theta_0\frac{C_{\mathrm{i}}}{C_{\mathrm{p}0}}+\frac{tan^2\theta_0}{(1-\alpha_0)}}{(1+\frac{C_{\mathrm{p}0}}{(1-\alpha_0)C_{\mathrm{i}}}+\frac{C_{\mathrm{p}0}}{\alpha_0 C_{\mathrm{i}}})^2+tan^2\theta_0}\cdot \\
& \frac{\Big[2tan\theta\frac{tan\theta}{\partial P}+2(\frac{C_{\mathrm{p}}}{\alpha C_{\mathrm{i}}}+\frac{C_{\mathrm{p}}}{(1-\alpha)C_{\mathrm{i}}}+1)(\frac{\partial C_{\mathrm{p}}}{\partial P}\frac{1}{C_{\mathrm{i}}\alpha}+\frac{\partial C_{\mathrm{p}}}{\partial P}\frac{1}{C_{\mathrm{i}}(1-\alpha)}-\frac{\partial\alpha}{\partial P}\frac{C_{\mathrm{p}}}{C_{\mathrm{i}}\alpha^2}+\frac{\partial\alpha}{\partial P}\frac{C_{\mathrm{p}}}{C_{\mathrm{i}}(1-\alpha)^2})\Big]}{(\frac{1}{\alpha}+\frac{C_{\mathrm{p}}}{C_{\mathrm{i}}(1-\alpha)\alpha})(1+\frac{C_{\mathrm{p}}}{\alpha C_{\mathrm{i}}}+\frac{C_{\mathrm{p}}}{(1-\alpha)C_{\mathrm{i}}})+\frac{tan^2\theta}{1-\alpha}+\frac{C_{\mathrm{i}}}{C_{\mathrm{p}}}tan^2\theta)^2}
\end{aligned}
\tag{B.34}
$$

Note that $\alpha|_{P=0}=\alpha_0,\ C_{\mathrm{p}}|_{P=0}=C_{\mathrm{p}0},\ tan\theta|_{P=0}=tan\theta_0$, Eqs. (A.3), (A.6–A.7), and (A.11), therefore, we have

$$
\begin{aligned}
S|_{P=0} = \frac{1}{E}\Bigg[& \frac{(\frac{1}{\alpha_0}+\frac{C_{\mathrm{p}0}}{\alpha_0(1-\alpha_0)C_{\mathrm{i}}})(\frac{C_{\mathrm{p}0}}{C_{\mathrm{i}}}\frac{-1}{(1-\alpha_0)^2})+[\frac{2(n-1)}{1-\alpha_0}-\frac{\alpha_0}{(1-\alpha_0)^2}+(2n-1)\frac{C_{\mathrm{i}}}{C_{\mathrm{p}0}}]tan^2\theta}{(\frac{C_{\mathrm{p}0}}{\alpha_0 C_{\mathrm{i}}}+\frac{C_{\mathrm{p}0}}{(1-\alpha_0)C_{\mathrm{i}}}+1)(\frac{1}{\alpha_0}+\frac{C_{\mathrm{p}0}}{(1-\alpha_0)\alpha_0 C_{\mathrm{i}}})+(\frac{C_{\mathrm{i}}}{C_{\mathrm{p}0}}+\frac{1}{1-\alpha_0})tan^2\theta_0}+ \\
& \frac{2\frac{C_{\mathrm{p}0}}{(1-\alpha_0)^2 C_{\mathrm{i}}}(\frac{C_{\mathrm{p}0}}{\alpha_0 C_{\mathrm{i}}}+\frac{C_{\mathrm{p}}}{(1-\alpha_0)C_{\mathrm{i}}}+1)-2(n-1)tan^2\theta_0}{(\frac{C_{\mathrm{p}}}{\alpha_0 C_{\mathrm{i}}}+\frac{C_{\mathrm{p}0}}{(1-\alpha_0)C_{\mathrm{i}}}+1)^2+tan^2\theta_0}\Bigg],
\end{aligned}
\tag{B.35}
$$

Substituting α_0 with α, $C_{\mathrm{p}0}$ with C_{p}, $tan\theta_0$ with $tan\theta$, we get the following.

$$
\begin{aligned}
S = \frac{1}{E}\Bigg[& \frac{(\frac{1}{\alpha}+\frac{C_{\mathrm{p}}}{\alpha(1-\alpha)C_{\mathrm{i}}})(\frac{C_{\mathrm{p}}}{C_{\mathrm{i}}}\frac{-1}{(1-\alpha)^2})+[\frac{2(n-1)}{1-\alpha}-\frac{\alpha}{(1-\alpha)^2}+(2n-1)\frac{C_{\mathrm{i}}}{C_{\mathrm{p}}}]tan^2\theta}{(\frac{C_{\mathrm{p}}}{\alpha C_{\mathrm{i}}}+\frac{C_{\mathrm{p}}}{(1-\alpha)C_{\mathrm{i}}}+1)(\frac{1}{\alpha}+\frac{C_{\mathrm{p}}}{(1-\alpha)\alpha C_{\mathrm{i}}})+(\frac{C_{\mathrm{i}}}{C_{\mathrm{p}}}+\frac{1}{1-\alpha})tan^2\theta}+ \\
& \frac{2\frac{C_{\mathrm{p}}}{(1-\alpha)^2 C_{\mathrm{i}}}(\frac{C_{\mathrm{p}}}{\alpha C_{\mathrm{i}}}+\frac{C_{\mathrm{p}}}{(1-\alpha)C_{\mathrm{i}}}+1)-2(n-1)tan^2\theta}{(\frac{C_{\mathrm{p}}}{\alpha C_{\mathrm{i}}}+\frac{C_{\mathrm{p}}}{(1-\alpha)C_{\mathrm{i}}}+1)^2+tan^2\theta}\Bigg],
\end{aligned}
\tag{B.36}
$$

Changing the phase angle θ with the loss angle δ, we can get the analytical solution Eq.17.

$$
\begin{aligned}
S = \frac{1}{E}\Bigg[& \frac{(\frac{1}{\alpha}+\frac{C_{\mathrm{p}}}{\alpha(1-\alpha)C_{\mathrm{i}}})(\frac{C_{\mathrm{p}}}{C_{\mathrm{i}}}\frac{-1}{(1-\alpha)^2})\cdot tan^2\delta+[\frac{2(n-1)}{1-\alpha}-\frac{\alpha}{(1-\alpha)^2}+(2n-1)\frac{C_{\mathrm{i}}}{C_{\mathrm{p}}}]}{(\frac{C_{\mathrm{p}}}{\alpha C_{\mathrm{i}}}+\frac{C_{\mathrm{p}}}{(1-\alpha)C_{\mathrm{i}}}+1)(\frac{1}{\alpha}+\frac{C_{\mathrm{p}}}{(1-\alpha)\alpha C_{\mathrm{i}}})\cdot tan^2\delta+(\frac{C_{\mathrm{i}}}{C_{\mathrm{p}}}+\frac{1}{1-\alpha})}+ \\
& \frac{2\frac{C_{\mathrm{p}}}{(1-\alpha)^2 C_{\mathrm{i}}}(\frac{C_{\mathrm{p}}}{\alpha C_{\mathrm{i}}}+\frac{C_{\mathrm{p}}}{(1-\alpha)C_{\mathrm{i}}}+1)\cdot tan^2\delta-2(n-1)}{(\frac{C_{\mathrm{p}}}{\alpha C_{\mathrm{i}}}+\frac{C_{\mathrm{p}}}{(1-\alpha)C_{\mathrm{i}}}+1)^2\cdot tan^2\delta+1}\Bigg],
\end{aligned}
\tag{B.37}
$$

We get the expression 17.

Appendix C. Comparison of previous model in (Ha et al., 2021; Li et al., 2022) and double branch model

According to the derivation in (Li et al., 2022), the normalized capacitance of HRPS can be expressed as follows:

$$\frac{C_{\mathrm{CPS}}}{C_{\mathrm{i}}} = \frac{tan^2\theta + 1}{tan^2\theta\frac{C_{\mathrm{i}}}{C_{\mathrm{p}}} + tan^2\theta + 1}. \tag{C.1}$$

where C_{HPRS} is the capacitance of HRPS, C_{i} is the capacitance of the capacitance of the dielectric layer.

Now we consider two states; C_{HRPS0} is the initial state (constant) and C_{HRPS} as a state under pressure.The normalized capacitance change could be written as:

$$\frac{\triangle C}{C_0} = \frac{C_{\mathrm{CPS}}}{C_{\mathrm{CPS0}}} - 1 = \frac{tan^2\theta + 1}{tan^2\theta\frac{C_{\mathrm{i}}}{C_{\mathrm{p}}} + tan^2\theta + 1}\frac{tan^2\theta_0\frac{C_{\mathrm{i}}}{C_{\mathrm{p0}}} + tan^2\theta_0 + 1}{tan^2\theta_0 + 1} - 1. \tag{C.2}$$

The sensitivity could be written as follows:

$$\frac{\partial(\frac{\triangle C}{C_0})}{\partial P} = \frac{\partial(\frac{C_{\mathrm{CPS}}}{C_{\mathrm{CPS0}}} - 1)}{\partial P} = \frac{1}{C_{\mathrm{CPS0}}}\frac{\partial(C_{\mathrm{CPS}})}{\partial P}. \tag{C.3}$$

$$\frac{\partial(\frac{\triangle C}{C_0})}{\partial P} = \frac{tan^2\theta_0\frac{C_{\mathrm{i}}}{C_{\mathrm{p0}}} + tan^2\theta_0 + 1}{tan^2\theta_0 + 1}\frac{\partial(\frac{tan^2\theta+1}{tan^2\theta\frac{C_{\mathrm{i}}}{C_{\mathrm{p}}}+tan^2\theta+1})}{\partial P}. \tag{C.4}$$

$$\frac{\partial(\frac{\triangle C}{C_0})}{\partial P} = (\frac{tan^2\theta_0\frac{C_{\mathrm{i}}}{C_{\mathrm{p}}} + tan^2\theta_0 + 1}{tan^2\theta_0 + 1})\cdot \frac{2tan\theta(\frac{\partial tan\theta}{\partial P})(tan^2\theta\frac{C_{\mathrm{i}}}{C_{\mathrm{p}}} + tan^2\theta + 1) - (tan^2\theta + 1)(2tan\theta\frac{C_{\mathrm{i}}}{C_{\mathrm{p}}}\frac{\partial tan\theta}{\partial P} + tan^2\theta C_{\mathrm{i}}\frac{\partial\frac{1}{C_{\mathrm{p}}}}{\partial P} + 2tan\theta\frac{\partial tan\theta}{\partial P})}{(tan^2\theta\frac{C_{\mathrm{i}}}{C_{\mathrm{p}}} + tan^2\theta + 1)^2} \tag{C.5}$$

Organizing it, we get:

$$\frac{\partial(\frac{\triangle C}{C_0})}{\partial P} = (\frac{tan^2\theta_0\frac{C_{\mathrm{i}}}{C_{\mathrm{p}}} + tan^2\theta_0 + 1}{tan^2\theta_0 + 1})\frac{-2tan\theta\frac{C_i}{C_{\mathrm{p}}}\frac{\partial tan\theta}{\partial P} - (tan\theta^2 + 1)tan\theta^2 C_{\mathrm{i}}\frac{\partial(\frac{1}{C_{\mathrm{p}}})}{\partial P}}{(tan\theta^2\frac{C_{\mathrm{i}}}{C_{\mathrm{p}}} + tan\theta^2 + 1)^2}. \tag{C.6}$$

Here, we derive the term $\frac{\partial\frac{1}{C_{\mathrm{p}}}}{\partial P}$:

$$\frac{\partial\frac{1}{C_{\mathrm{p}}}}{\partial P} = \frac{1}{k\epsilon_0 A}\frac{\partial d}{\partial\varepsilon}\frac{\partial\varepsilon}{\partial P}. \tag{C.7}$$

$$\left.\frac{\partial\frac{1}{C_{\mathrm{p}}}}{\partial P}\right|_{P=0} = \frac{1}{k\epsilon_0 A}(-d_0)(\frac{1}{E}) = -\frac{1}{C_{\mathrm{p}}E}. \tag{C.8}$$

Plugging it into the corresponding expression:

$$\left.\frac{\partial(\frac{\triangle C}{C_0})}{\partial P}\right|_{P=0} = (\frac{tan^2\theta_0\frac{C_{\mathrm{i}}}{C_{\mathrm{p0}}} + tan^2\theta_0 + 1}{tan^2\theta_0 + 1})\frac{-2tan\theta_0\frac{C_i}{C_{\mathrm{p0}}}\frac{(1-n)}{E}tan\theta_0 - (tan^2\theta_0 + 1)tan^2\theta_0 C_{\mathrm{i}}(\frac{-1}{C_{\mathrm{p0}}E})}{(tan^2\theta_0\frac{C_{\mathrm{i}}}{C_{\mathrm{p0}}} + tan^2\theta_0 + 1)^2}. \tag{C.9}$$

Substitute θ_0 with θ, and C_{p0} with C_{p}

$$= \frac{1}{E}\left[\frac{1}{tan^2\theta + 1}\frac{2tan^2\theta\frac{C_{\mathrm{i}}}{C_{\mathrm{p}}}(n-1)}{(tan^2\theta\frac{C_{\mathrm{i}}}{C_{\mathrm{p}}} + tan^2\theta + 1)} + \frac{tan^2\theta\frac{C_{\mathrm{i}}}{C_{\mathrm{p}}}}{(tan^2\theta\frac{C_{\mathrm{i}}}{C_{\mathrm{p}}} + tan^2\theta + 1)}\right]. \tag{C.10}$$

Replace phase angle θ with loss angle δ:

$$= \frac{1}{E}\left[\frac{tan^2\delta}{tan^2\delta + 1}\frac{2\frac{C_{\mathrm{i}}}{C_{\mathrm{p}}}(n-1)}{(\frac{C_{\mathrm{i}}}{C_{\mathrm{p}}} + 1 + tan^2\delta)} + \frac{\frac{C_{\mathrm{i}}}{C_{\mathrm{p}}}}{(\frac{C_{\mathrm{i}}}{C_{\mathrm{p}}} + 1 + tan^2\delta)}\right]. \tag{C.11}$$

We plot the circuit model used in (Ha et al., 2021; Li et al., 2022) and compare it with the generalized double-branch model developed in this work, using representative parameters: Young's modulus of the sensing material $E = 2.18$ kPa, Archie's law coefficient $n = 4$, capacitance ratio $C_{\mathrm{i}}/C_{\mathrm{p}} = 1000$, and contact ratio $\alpha = 0.14$.

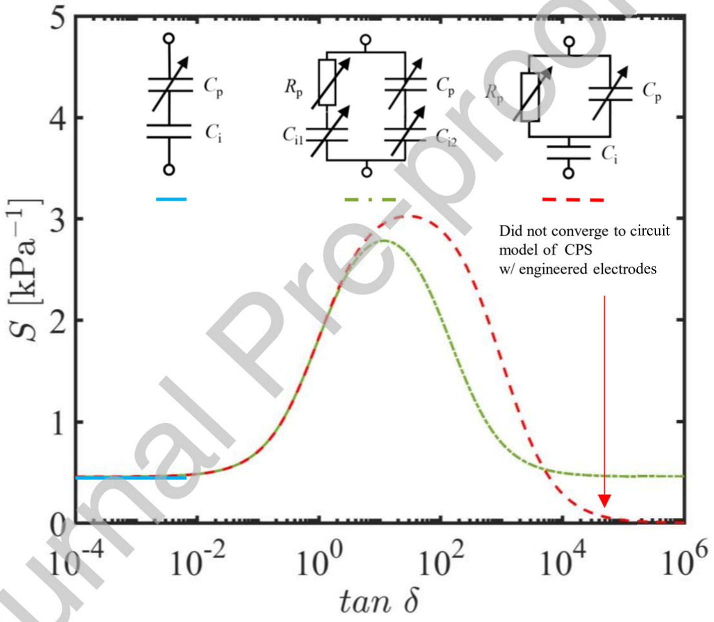

Figure C.2: Comparison between the previous model (Ha et al., 2021; Li et al., 2022) and the generalized double-branch model developed in this work. The two models show good agreement in the small to intermediate loss-tangent regime. However, the previous model fails to capture the sensitivity in the limit of CPS with engineered electrodes.

As shown in Fig. C.2, the previous model fails to converge to the case of CPS with engineered electrodes when loss angle δ of the sensing layer $\sim 90°$, indicating that it is not sufficiently general.

Appendix D. Derivation of Two Sympotic Boundaries

To clearly delineate the conditions under which the generalized double-branch model reduces to the simpler single-branch cases, we derive the asymptotic boundaries by comparing their respective sensitivity expressions.

Appendix D.1. Sensitivity Expressions for the Circuit Models

For a CPS, the sensitivity S is defined in terms of the normalized capacitance variation with respect to the applied pressure. Based on the proposed equivalent circuit models:

1. **Double branch model** (generalized case):

$$S = f(E, tan\ \delta, \frac{C_\mathrm{i}}{C_\mathrm{p}}, \alpha, n), \tag{D.1}$$

where E is Young's modulus, θ is the phase angle, $C_\mathrm{i}/C_\mathrm{p}$ is the capacitance ratio, n is Archie's law coefficient and α is the contact ratio.

2. **Single branch model** (engineered dielectrics):

$$S = \frac{1}{E}\frac{\frac{C_\mathrm{i}}{C_\mathrm{p}}}{1+\frac{C_\mathrm{i}}{C_\mathrm{p}}}, \tag{D.2}$$

3. **Single branch model** (engineered electrodes):

$$S = \frac{1}{E}, \tag{D.3}$$

The single-branch capacitor and resistor models can be regarded as special cases of the double-branch formulation, corresponding, respectively, to $\theta = -90°$ (purely capacitive) and $\theta = 0°$ (purely resistive).

Appendix D.2. Boundary Conditions

To determine the boundaries that separate the different regimes, we equate the generalized sensitivity expression (Eq. D.1) with each of the single-branch cases:

$$f(E, tan\ \delta, \frac{C_\mathrm{i}}{C_\mathrm{p}}, \alpha, n) = \frac{1}{E}\frac{\frac{C_\mathrm{i}}{C_\mathrm{p}}}{1+\frac{C_\mathrm{i}}{C_\mathrm{p}}}, \tag{D.4}$$

$$f(E, tan\ \delta, \frac{C_\mathrm{i}}{C_\mathrm{p}}, \alpha, n) = \frac{1}{E}. \tag{D.5}$$

Solving Eqs. D.4–D.5 for $\tan\delta$ yields two critical boundary conditions that demarcate the transitions between regimes. The Eqs. D.4–D.5 is solved through MATLAB.

Appendix D.3. Asymptotic Reduction

In our experiment $\frac{C_\mathrm{i}}{C_\mathrm{p}}$ is much larger than 10, therefore $\frac{C_\mathrm{i}}{C_\mathrm{p}}$ is chosen to be the main variable, therefore we did a Taylor expansion regarding the solution and simplified the boundaries.

$$tan\ \delta \sim \frac{1}{\sqrt{\frac{C_\mathrm{i}}{C_\mathrm{p}}}}\sqrt{\frac{2\alpha}{n(1-\alpha)}}, \tag{D.6}$$

$$\tan\ \delta \sim \frac{C_\mathrm{i}}{C_\mathrm{p}}\sqrt{\frac{n\alpha}{4(1-\alpha)}}. \tag{D.7}$$

Appendix D.4. Physical Interpretation

Equations D.6–D.7 define the left and right asymptotic boundaries observed in Fig. 4. These boundaries provide a mechanistic criterion for when the double-branch model collapses to either of the single-branch models:

- For $\tan\delta \to 0$, the system behaves as a CPS with engineered dielectrics.
- For $\tan\delta \to \infty$, the system reduces to a CPS with engineered electrodes.
- In the intermediate regime bounded by Eqs. D.6–D.7, both capacitive and resistive branches contribute significantly, corresponding to HRPS.

Doping ratio	$\frac{C_i}{C_p}$	n	α	Experiment δ	$\delta \sim \frac{1}{\sqrt{\frac{C_i}{C_p}}}\sqrt{\frac{2\alpha}{n(1-\alpha)}}$	$\delta \sim \frac{C_i}{C_p}\sqrt{\frac{n\alpha}{4(1-\alpha)}}$	Type of Sensor
0% avg	$\frac{1.195\ \text{nF}}{4.05\ \text{pF}}$	0	0.14	1°	NA	NA	CPS w/ engineered dielectrics
0.2% avg	$\frac{1.195\ nF}{7.78\ \text{pF}}$	3.02	0.14	26.54°	1.52°	89.19°	1.52°<-26.54°<89.19° (HRPS)
0.4% avg	$\frac{1.195\ nF}{11.94\ \text{pF}}$	4.02	0.14	56.36°	1.63°	88.58°	1.63°<56.36°<88.58° (HRPS)
0.6% avg	$\frac{1.195\ nF}{31.39\ \text{pF}}$	3.42	0.14	85.74°	2.86°	86.56°	2.86°<85.74°<86.56° (HRPS)
0.8% avg	$\frac{1.195\ nF}{41.92\ \text{pF}}$	3.12	0.14	89.36°	3.46°	85.62°	3.46°<85.62°<89.36° (CPS w/ engineered electrodes)

Table D.4: Doping ratio, capacitance ratio $\frac{C_\mathrm{i}}{C_\mathrm{p}}$, phase angle δ, Archie's law exponent n, and contact ratio α of porous nanocomposites (PNC); the corresponding asymptotic boundaries that determine the sensor type; and the classification of sensor types at different doping ratios under an excitation frequency of 1 kHz and applied pressure of 1 kPa.

Thus, the asymptotic boundaries provide a predictive framework for mapping material parameters $(E, n, \alpha, C_\mathrm{i}/C_\mathrm{p})$ and electromechanical response (δ) to distinct sensor operation regimes. The asymptotic boundaries indicate that the most critical parameter for determining whether a sensor behaves as a CPS with engineered dielectrics, a hybrid response pressure sensor, or a CPS with engineered electrodes is the phase angle (δ or tan δ) of the sensing material. Although the phase angle of a given sensing material is intrinsic and cannot be altered after fabrication, sensor sensitivity can still be tuned by adjusting the dielectric layer thickness (i.e., modifying C_i). By substituting the relevant parameters for each doping ratio into the corresponding asymptotic boundaries, the results can be summarized in the following table. From this analysis, we therefore conclude that 0% doping ratio is Engineered electrodes, 0.8% is the engineered electrodes, 0.2%, 0.4%, and 0.6% are hybrid response.

Bibliography

References

Bai, N., Wang, L., Wang, Q., Deng, J., Wang, Y., Lu, P., Huang, J., Li, G., Zhang, Y., Yang, J., et al., 2020. Graded intrafillable architecture-based iontronic pressure sensor with ultra-broad-range high sensitivity. Nature communications 11, 209.

Bai, N., Wang, L., Xue, Y., Wang, Y., Hou, X., Li, G., Zhang, Y., Cai, M., Zhao, L., Guan, F., et al., 2022. Graded interlocks for iontronic pressure sensors with high sensitivity and high linearity over a broad range. Acs Nano 16, 4338–4347.

Barrau, S., Demont, P., Peigney, A., Laurent, C., Lacabanne, C., 2003. Dc and ac conductivity of carbon nanotubes- polyepoxy composites. Macromolecules 36, 5187–5194.

Berman, A., Hsiao, K., Root, S.E., Choi, H., Ilyn, D., Xu, C., Stein, E., Cutkosky, M., DeSimone, J.M., Bao, Z., 2024. Additively manufactured micro-lattice dielectrics for multiaxial capacitive sensors. Science Advances 10, eadq8866.

Bilent, S., Dinh, T.H.N., Martincic, E., Joubert, P.Y., 2019. Influence of the porosity of polymer foams on the performances of capacitive flexible pressure sensors. Sensors (Basel) 19. URL: `https://www.ncbi.nlm.nih.gov/pubmed/31035496`, doi:`10.3390/s19091968`.

Chen, W., Yan, X., 2020. Progress in achieving high-performance piezoresistive and capacitive flexible pressure sensors: A review. Journal of Materials Science and Technology 43, 175–188. URL: `https://www.sciencedirect.com/science/article/pii/S100503022030044X`, doi:`https://doi.org/10.1016/j.jmst.2019.11.010`.

Choi, W., Lee, J., Kyoung Yoo, Y., Kang, S., Kim, J., Hoon Lee, J., 2014. Enhanced sensitivity of piezoelectric pressure sensor with microstructured polydimethylsiloxane layer. Applied Physics Letters 104, 123701.

Chorsi, M.T., Curry, E.J., Chorsi, H.T., Das, R., Baroody, J., Purohit, P.K., Ilies, H., Nguyen, T.D., 2019. Piezoelectric biomaterials for sensors and actuators. Advanced Materials 31, 1802084.

Chortos, A., Liu, J., Bao, Z., 2016. Pursuing prosthetic electronic skin. Nature materials 15, 937–950.

Chun, J., Lee, K.Y., Kang, C.Y., Kim, M.W., Kim, S.W., Baik, J.M., 2014. Embossed hollow hemisphere-based piezoelectric nanogenerator and highly responsive pressure sensor. Advanced Functional Materials 24, 2038–2043.

Dahiya, R.S., Mittendorfer, P., Valle, M., Cheng, G., Lumelsky, V.J., 2013. Directions toward effective utilization of tactile skin: A review. IEEE Sensors Journal 13, 4121–4138.

Duan, Y., He, S., Wu, J., Su, B., Wang, Y., 2022. Recent progress in flexible pressure sensor arrays. Nanomaterials 12, 2495.

Feng, Z., He, Q., Wang, X., Lin, Y., Qiu, J., Wu, Y., Yang, J., 2023. Capacitive sensors with hybrid dielectric structures and high sensitivity over a wide pressure range for monitoring biosignals. ACS Applied Materials & Interfaces 15, 6217–6227.

Garcia, C., Trendafilova, I., de Villoria, R.G., del Rio, J.S., 2018. Self-powered pressure sensor based on the triboelectric effect and its analysis using dynamic mechanical analysis. Nano Energy 50, 401–409.

Ha, K.H., Huh, H., Li, Z., Lu, N., 2022. Soft capacitive pressure sensors: trends, challenges, and perspectives. ACS nano 16, 3442–3448.

Ha, K.H., Li, Z., Kim, S., Huh, H., Wang, Z., Shi, H., Block, C., Bhattacharya, S., Lu, N., 2024. Stretchable hybrid response pressure sensors. Matter 7, 1895–1908.

Ha, K.H., Zhang, W., Jang, H., Kang, S., Wang, L., Tan, P., Hwang, H., Lu, N., 2021. Highly sensitive capacitive pressure sensors over a wide pressure range enabled by the hybrid responses of a highly porous nanocomposite. Advanced Materials 33, 2103320.

He, K., Hou, Y., Yi, C., Li, N., Sui, F., Yang, B., Gu, G., Li, W., Wang, Z., Li, Y., et al., 2020. High-performance zero-standby-power-consumption-under-bending pressure sensors for artificial reflex arc. Nano Energy 73, 104743.

He, S., Wu, J., Su, B., Liu, S., Wang, Y., 2023. Design of pdms/cnt flexible pressure sensor based on double structure with the regulation of electrical properties. Composites Science and Technology 242, 110166.

Javidi, R., Moghimi Zand, M., Alizadeh Majd, S., 2023. Designing wearable capacitive pressure sensors with arrangement of porous pyramidal microstructures. Micro and Nano Systems Letters 11. doi:`10.1186/s40486-023-00178-7`.

Jin, Q., Wang, C., Wu, H., Luo, X., Li, J., Ma, G., Li, Y., Luo, C., Guo, F., Long, Y., 2024. 3d printing of capacitive pressure sensors with tuned wide detection range and high sensitivity inspired by bio-inspired kapok structures. Macromolecular Rapid Communications 45, 2300668.

Kang, J.H., Park, C., Scholl, J.A., Brazin, A.H., Holloway, N.M., High, J.W., Lowther, S.E., Harrison, J.S., 2009. Piezoresistive characteristics of single wall carbon nanotube/polyimide nanocomposites. Journal of Polymer Science Part B: Polymer Physics 47, 994–1003.

Lee, S., Reuveny, A., Reeder, J., Lee, S., Jin, H., Liu, Q., Yokota, T., Sekitani, T., Isoyama, T., Abe, Y., et al., 2016. A transparent bending-insensitive pressure sensor. Nature nanotechnology 11, 472–478.

Lee, W.W., Tan, Y.J., Yao, H., Li, S., See, H.H., Hon, M., Ng, K.A., Xiong, B., Ho, J.S., Tee, B.C., 2019. A neuro-inspired artificial peripheral nervous system for scalable electronic skins. Science Robotics 4, eaax2198.

Lee, Y., Park, J., Cho, S., Shin, Y.E., Lee, H., Kim, J., Myoung, J., Cho, S., Kang, S., Baig, C., et al., 2018. Flexible ferroelectric sensors with ultrahigh pressure sensitivity and linear response over exceptionally broad pressure range. ACS nano 12, 4045–4054.

Li, J., Fang, L., Sun, B., Li, X., Kang, S.H., 2020a. Recent progress in flexible and stretchable piezoresistive sensors and their applications. Journal of the Electrochemical Society 167, 037561.

Li, R., Si, Y., Zhu, Z., Guo, Y., Zhang, Y., Pan, N., Sun, G., Pan, T., 2017. Supercapacitive iontronic nanofabric sensing. Advanced Materials 29, 1700253.

Li, S., Zhang, Y., Wang, Y., Xia, K., Yin, Z., Wang, H., Zhang, M., Liang, X., Lu, H., Zhu, M., et al., 2020b. Physical sensors for skin-inspired electronics. InfoMat 2, 184–211.

Li, Z., Ha, K.H., Wang, Z., Kim, S., Davis, B., Lu, R., Sirohi, J., Lu, N., 2022. Effects of ac frequency on the capacitance measurement of hybrid response pressure sensors. Soft Matter 18, 8476–8485.

Li, Z., Kim, S., Wang, Z., Zhu, Z., Lu, N., 2024. Electromechanics of soft resistive and capacitive tactile sensors. Mechanics of Flexible and Stretchable Electronics , 373–430.

Li, Z., Wang, S., Ding, W., Chen, Y., Chen, M., Zhang, S., Liu, Z., Yang, W., Li, Y., 2023. Mechanically robust, flexible hybrid tactile sensor with microstructured sensitive composites for human-cyber-physical systems. Composites Science and Technology 244, 110303.

Liu, M., Pu, X., Jiang, C., Liu, T., Huang, X., Chen, L., Du, C., Sun, J., Hu, W., Wang, Z.L., 2017. Large-area all-textile pressure sensors for monitoring human motion and physiological signals. Advanced materials 29, 1703700.

Lu, X., Yvonnet, J., Detrez, F., Bai, J., 2017. Multiscale modeling of nonlinear electric conductivity in graphene-reinforced nanocomposites taking into account tunnelling effect. Journal of Computational Physics 337, 116–131.

Luan, X., Zhu, Y., Chen, Y., Gu, X., Xu, Q., Liu, G., Zhang, X., Kuang, M., 2024. Biodegradable pressure sensors with high sensitivity and wide detection range via a piezoresistive/capacitive dual response. Polymer Chemistry 15, 4972–4981.

Man, J., Chen, G., Chen, J., 2022. Recent progress of biomimetic tactile sensing technology based on magnetic sensors. Biosensors 12, 1054.

Mannsfeld, S.C., Tee, B.C., Stoltenberg, R.M., Chen, C.V.H., Barman, S., Muir, B.V., Sokolov, A.N., Reese, C., Bao, Z., 2010. Highly sensitive flexible pressure sensors with microstructured rubber dielectric layers. Nature materials 9, 859.

Meng, K., Xiao, X., Wei, W., Chen, G., Nashalian, A., Shen, S., Xiao, X., Chen, J., 2022. Wearable pressure sensors for pulse wave monitoring. Advanced Materials 34, 2109357.

Mishra, R.B., El-Atab, N., Hussain, A.M., Hussain, M.M., 2021a. Recent progress on flexible capacitive pressure sensors: From design and materials to applications. Advanced materials technologies 6, 2001023.

Mishra, R.B., El-Atab, N., Hussain, A.M., Hussain, M.M., 2021b. Recent progress on flexible capacitive pressure sensors: From design and materials to applications. Advanced Materials Technologies 6. doi:`10.1002/admt.202001023`.

Nie, Z., Kwak, J.W., Han, M., Rogers, J.A., 2024. Mechanically active materials and devices for bio-interfaced pressure sensors—a review. Advanced Materials 36, 2205609.

Park, S., Kim, H., Vosgueritchian, M., Cheon, S., Koo, J.H., Kim, T.R., Lee, S., Schwartz, G., Chang, H., Bao, Z., 2014. Stretchable energy-harvesting tactile electronic skin capable of differentiating multiple mechanical stimuli modes. Advanced materials (Deerfield Beach, Fla.) 26, 7324–7332.

Peng, S.H., Blanloeuil, P., Wu, S.Y., Wang, C.H., 2018. Rational design of ultrasensitive pressure sensors by tailoring microscopic features. Advanced Materials Interfaces 5. URL: `<GotoISI>://WOS:000445175500009`, doi:`10.1002/admi.201800403`.

Pyo, S., Lee, J., Bae, K., Sim, S., Kim, J., 2021a. Recent progress in flexible tactile sensors for human-interactive systems: from sensors to advanced applications. Advanced Materials 33, 2005902.

Pyo, S., Lee, J., Bae, K., Sim, S., Kim, J., 2021b. Recent progress in flexible tactile sensors for human-interactive systems: from sensors to advanced applications. Advanced Materials 33, 2005902.

Qin, J., Yin, L.J., Hao, Y.N., Zhong, S.L., Zhang, D.L., Bi, K., Zhang, Y.X., Zhao, Y., Dang, Z.M., 2021. Flexible and stretchable capacitive sensors with different microstructures. Advanced Materials 33, 2008267.

Qu, X., Li, J., Han, Z., Liang, Q., Zhou, Z., Xie, R., Wang, H., Chen, S., 2023. Highly sensitive fiber pressure sensors over a wide pressure range enabled by resistive-capacitive hybrid response. ACS nano 17, 14904–14915.

Ramuz, M., Tee, B., Tok, J., Bao, Z., 2012. Transparent, optical, pressure-sensitive artificial skin for large-area stretchable electronics. Advanced materials (Deerfield Beach, Fla.) 24, 3223–3227.

Ruth, S.R.A., Beker, L., Tran, H., Feig, V.R., Matsuhisa, N., Bao, Z., 2020. Rational design of capacitive pressure sensors based on pyramidal microstructures for specialized monitoring of biosignals. Advanced functional materials 30, 1903100.

Shang, E., Zhao, Z., Peng, S., Zhang, N., Fan, D., Liu, Y., 2025. Flexible linkage design of composite dielectric layer for high-performance capacitive pressure sensor. ACS Applied Electronic Materials .

Tee, B.C.K., Chortos, A., Dunn, R.R., Schwartz, G., Eason, E., Bao, Z., 2014. Tunable flexible pressure sensors using microstructured elastomer geometries for intuitive electronics. Advanced Functional Materials 24, 5427–5434.

Thouti, E., Chauhan, K., Prajesh, R., Farman, M., Maurya, R.K., Sharma, P., Nagaraju, A., 2022. Flexible capacitive pressure sensors using microdome like structured polydimethylsiloxane dielectric layers. Sensors and Actuators A: Physical 335, 113393.

Totaro, M., Bernardeschi, I., Wang, H., Beccai, L., 2020. Analysis and optimization of fully foam-based capacitive sensors, in: 2020 3rd IEEE International Conference on Soft Robotics (RoboSoft), IEEE. pp. 470–475.

Viry, L., Levi, A., Totaro, M., Mondini, A., Mattoli, V., Mazzolai, B., Beccai, L., 2014. Flexible three-axial force sensor for soft and highly sensitive artificial touch. Advanced materials 26, 2659–2664.

Wang, L., Yang, J., Cheng, W., Zou, J., Zhao, D., 2021a. Progress on polymer composites with low dielectric constant and low dielectric loss for high-frequency signal transmission. Frontiers in Materials 8, 774843.

Wang, M., Luo, Y., Wang, T., Wan, C., Pan, L., Pan, S., He, K., Neo, A., Chen, X., 2021b. Artificial skin perception. Advanced Materials 33, 2003014.

Wang, Z., Li, Z., Sun, S., Kim, S., Feng, X., Shi, H., Lu, N., 2024. Electromechanics of stretchable hybrid response pressure sensors based on porous nanocomposites. Journal of the Mechanics and Physics of Solids 193, 105872.

Xia, X., Zhong, Z., Weng, G.J., 2017. Maxwell–wagner–sillars mechanism in the frequency dependence of electrical conductivity and dielectric permittivity of graphene-polymer nanocomposites. Mechanics of Materials 109, 42–50.

Xiao, Y., Wu, X., Yang, L., Zhu, J., 2026. Fabrication of high-performance fabric-based capacitive pressure sensors with two-scale synergistic resistive/capacitive hybrid response. Journal of Materials Science & Technology 240, 87–97.

Xiong, Y., Han, J., Wang, Y., Wang, Z.L., Sun, Q., 2022. Emerging iontronic sensing: materials, mechanisms, and applications. Research .

Xiong, Y., Shen, Y., Tian, L., Hu, Y., Zhu, P., Sun, R., Wong, C.P., 2020. A flexible, ultra-highly sensitive and stable capacitive pressure sensor with convex microarrays for motion and health monitoring. Nano energy 70, 104436.

Yamada, Y., Morizono, T., Umetani, Y., Takahashi, H., 2005. Highly soft viscoelastic robot skin with a contact object-location-sensing capability. IEEE Transactions on Industrial electronics 52, 960–968.

Yang, H., Yuan, L., Yao, X., Fang, D., 2020. Piezoresistive response of graphene rubber composites considering the tunneling effect. Journal of the Mechanics and Physics of Solids 139, 103943.

Yang, T., Xie, D., Li, Z., Zhu, H., 2017. Recent advances in wearable tactile sensors: Materials, sensing mechanisms, and device performance. Materials Science and Engineering: R: Reports 115, 1–37.

Yao, S., Zhu, Y., 2014. Wearable multifunctional sensors using printed stretchable conductors made of silver nanowires. Nanoscale 6, 2345–2352.

Yuan, X., Won, S.M., Han, M., Wang, Y., Rogers, J.A., Huang, Y., Wang, H., 2021. Mechanics of encapsulated three-dimensional structures for simultaneous sensing of pressure and shear stress. Journal of the Mechanics and Physics of Solids 151, 104400.

Zang, Y., Zhang, F., Di, C.a., Zhu, D., 2015. Advances of flexible pressure sensors toward artificial intelligence and health care applications. Materials Horizons 2, 140–156.

Zhang, H., Weng, L., Yang, H., Hao, L., Zuo, S., Wang, M., Huang, X., Wang, S., 2025. Flexible dual-mode capacitive tactile sensor with wide linear range based on three-level gradient micro-dome porous structure. Sensors and Actuators A: Physical , 117440.

Zhang, J., Wang, Z., Peng, Z., 2021. Analytical model of the piezoresistive behavior of highly compressible sensors made of microporous nanocomposites. Advanced Theory and Simulations 4, 2100247.

Zhang, Y., Hu, Y., Zhu, P., Han, F., Zhu, Y., Sun, R., Wong, C.P., 2017. Flexible and highly sensitive pressure sensor based on microdome-patterned pdms forming with assistance of colloid self-assembly and replica technique for wearable electronics. ACS applied materials interfaces 9, 35968–35976.

Zhang, Y., Lin, Z., Huang, X., You, X., Ye, J., Wu, H., 2019a. Highly sensitive capacitive pressure sensor with elastic metallized sponge. Smart Materials and Structures 28. doi:`10.1088/1361-665X/ab3a0c`.

Zhang, Y., Lin, Z., Huang, X., You, X., Ye, J., Wu, H., 2019b. Highly sensitive capacitive pressure sensor with elastic metallized sponge. Smart Materials and Structures 28, 105023.

Zhao, L., Qiang, F., Dai, S.W., Shen, S.C., Huang, Y.Z., Huang, N.J., Zhang, G.D., Guan, L.Z., Gao, J.F., Song, Y.H., et al., 2019. Construction of sandwich-like porous structure of graphene-coated foam composites for ultrasensitive and flexible pressure sensors. Nanoscale 11, 10229–10238.

Zhao, Y., Ruan, X., Hao, J., Liu, H., Mou, S., Zhu, X., Qiu, J., Wang, X., Li, C., Lv, C., et al., 2025. Easily fabricated flexible pressure sensor with angelfish-structured zno/sr dielectric layer for human–machine interaction. ACS Applied Bio Materials 8, 9439–9450.

Zheng, Z., Pan, Y., Huang, H., 2025. A capacitive pressure sensor with a hierarchical microporous scaffold prepared by melt near-field electro-writing. Sensors 25, 2814.

Zhong, Y., Gu, F., Wu, L., Wang, J., Dai, S., Zhu, H., Cheng, G., Ding, J., 2023. Porous conductive electrode for highly sensitive flexible capacitive pressure sensor over a wide range. Journal of Alloys and Compounds 934, 167919.